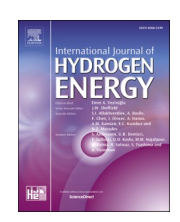
ELSEVIER

Contents lists available at ScienceDirect

# International Journal of Hydrogen Energy

journal homepage: www.elsevier.com/locate/he





# Enhanced glycerol steam reforming using Ni-doped CaZrO<sub>3</sub>, SrZrO<sub>3</sub>, and BaZrO<sub>3</sub> perovskite oxides

Igor Luisetto <sup>a</sup>, Nikolaos D. Charisiou <sup>b,\*</sup> , Anastasios I. Tsiotsias <sup>b</sup>, Angeliki I. Latsiou <sup>b</sup>, Georgios Siakavelas <sup>b</sup>, Victor Sebastian <sup>c,d,e</sup>, Runduo Zhang <sup>f</sup>, Elisabetta Di Bartolomeo <sup>g</sup>, Kyriaki Polychronopoulou <sup>h,i</sup>, Maria A. Goula <sup>b,\*\*</sup>

- <sup>a</sup> Department of Energy Technologies, Production, Conversion and Efficient Use of Energy Division, Process and Energy Systems Engineering Laboratory, ENEA Research Center, Casaccia, S.M. di Galeria, 00123, Rome, Italy
- b Laboratory of Alternative Fuels and Environmental Catalysis (LAFEC), Department of Chemical Engineering, University of Western Macedonia, GR-50100, Greece
- c Department of Chemical Engineering and Environmental Technology, Universidad de Zaragoza, Campus Río Ebro-Edificio I+D, 50018, Zaragoza, Spain
- d Instituto de Nanociencia y Materiales de Aragón (INMA), Universidad de Zaragoza- CSIC, c/ María de Luna 3, 50018, Zaragoza, Spain
- e Networking Research Center on Bioengineering, Biomaterials and Nanomedicine, CIBERBBN, 28029, Madrid, Spain
- f State Key Laboratory of Chemical Resource Engineering, Beijing Key Laboratory of Energy Environmental Catalysis, Beijing University of Chemical Technology, Beijing, 100029, China
- g Department of Chemical Science and Technologies, University of Rome Tor Vergata, Via della Ricerca Scientifica 1, 00133, Rome, Italy
- h Center for Catalysis and Separations, Khalifa University of Science and Technology, Abu Dhabi, P.O. Box 127788, United Arab Emirates
- Department of Mechanical Engineering, Khalifa University of Science and Technology, Abu Dhabi, P.O. Box 127788, United Arab Emirates

#### ARTICLE INFO

Handling Editor: Suleyman I. Allakhverdiev

Keywords:
Glycerol steam reforming
Alkaline earth metal zirconate perovskites
Nickel catalysts
Exsolution
Hydrogen production

# ABSTRACT

This study investigates the catalytic activity and time-on-stream stability of Ni catalysts supported on CaZrO<sub>3</sub>, SrZrO3, and BaZrO3 perovskite oxides for the glycerol steam reforming (GSR) reaction, which aims to convert the crude glycerol obtained from the transesterification of vegetable and microalgae oils (during bio-diesel production) into hydrogen gas. We employed XRD, N2 physisorption, H2-TPR, H2 pulse chemisorption, CO2-TPD, Raman, TPO, and TEM/HAADF-STEM to examine the surface and bulk properties of the catalysts before and after the reaction. Regarding catalytic activity evaluation, the Ni catalysts supported on CaZrO3 and SrZrO3 can effectively eliminate all liquid products (acetol, acetone, allyl alcohol, acetaldehyde, and acetic acid) at reaction temperatures higher than 500  $^{\circ}$ C, converting all glycerol to gaseous products (>6 mol H<sub>2</sub>/mol of glycerol for the best performing Ni/SrZrO<sub>3</sub>). This is due to a higher Ni dispersion, increased availability of active sites for the dissociation of C<sub>3</sub>H<sub>8</sub>O and H<sub>2</sub>O molecules, and a more favorable and stronger Ni-support interaction. Notably, the activity of Ni supported on SrZrO3 is among the highest reported in the literature. Furthermore, due to its unique Ni-support interaction, the Ni catalyst supported on SrZrO3 demonstrated remarkable catalytic stability.  $Apparently, some\ Ni^{2+}\ cations\ are\ solubilized\ into\ the\ perovskite\ lattice\ following\ high-temperature\ calcination.$ After being incorporated into the perovskite lattice, these cations then migrate to the surface via the exsolution process upon high-temperature reduction. During the glycerol steam reforming reaction, this helps prevent carbon growth on the exposed metallic Ni surface, thereby prolonging the catalyst lifetime and ensuring reliable H<sub>2</sub> production during long-term operation and under harsh reaction conditions.

#### 1. Introduction

Rapid industrialization worldwide has increased our reliance on

petroleum-based fuels, leading to an unprecedented increase in  ${\rm CO_2}$  emissions. This has raised significant concerns about the impact of global warming and climate change, necessitating the development of

E-mail addresses: ncharisiou@uowm.gr (N.D. Charisiou), mgoula@uowm.gr (M.A. Goula).

#### https://doi.org/10.1016/j.ijhydene.2025.04.246

Received 21 June 2024; Received in revised form 18 March 2025; Accepted 14 April 2025 Available online 18 April 2025

0360-3199/© 2025 Hydrogen Energy Publications LLC. Published by Elsevier Ltd. All rights are reserved, including those for text and data mining, AI training, and similar technologies.

<sup>\*</sup> Corresponding author. University of Western Macedonia, Department of Chemical Engineering, Laboratory of Alternative Fuels and Environmental Catalysis, ZEP, Kozani, 50100, Greece.

<sup>\*\*</sup> Corresponding author. University of Western Macedonia, Department of Chemical Engineering, Laboratory of Alternative Fuels and Environmental Catalysis, ZEP, Kozani, 50100, Greece.

alternative or carbon-neutral energy sources and feedstocks [1–3]. Biofuels have emerged as an attractive alternative to fossil fuels and are considered a bridge fuel in the transition towards a green, circular economy [4–6]. Among biofuels, biodiesel, produced through the transesterification of vegetable oils, shows great promise as a green substitute for oil-derived heavy fuels [7–9].

A common by-product of the transesterification process is crude glycerol, which constitutes about 10 % of the volume. This crude glycerol requires expensive refining to be commercially viable [10,11]. Alternatively, crude glycerol can be converted into hydrogen through various thermochemical processes, which include aqueous phase reforming (APR), auto thermal reforming (ATR), supercritical water reforming (SCWR), and glycerol steam reforming (GSR) [12,13]. Among them, GSR is a more mature technology and can produce a significantly higher amount of hydrogen per mole of converted glycerol (theoretically 7 mol) [14,15]. The overall GSR reaction is described by Eq. (1), and it can be considered as a combination of glycerol decomposition (GD, Eq. (2)) and water-gas shift (WGS, Eq. (3)). However, the overall process is complex, with numerous accompanying side-reactions that can occur depending on the reaction conditions, such as CO/CO2 methanation, methane dry/steam reforming, methane decomposition, Boudouard reaction and others [16-18].

**GSR:** 
$$C_3H_8O_3 + 3H_2O \rightarrow 3CO_2 + 7H_2$$
  $\Delta_rH = + 123 \text{ kJ/mol}$  (1)

**GD:** 
$$C_3H_8O_3 \rightarrow 3CO + 4H_2$$
  $\Delta_rH = +245 \text{ kJ/mol}$  (2)

WGS: 
$$CO + H_2O \rightarrow CO_2 + H_2$$
  $\Delta_r H = -41 \text{ kJ/mol}$  (3)

Thermodynamic studies have indicated that maximizing hydrogen yield is favored at atmospheric pressure and high water-to-glycerol feed ratios (WGFR >9:1) [18,19]. An active GSR catalyst should promote the splitting of C-H, C-C, and O-H bonds (through glycerol decomposition and water-gas shift) [19,20]. In practice, a significant amount of liquid by-products (such as acetone, acetol, allyl alcohol, acetaldehyde, acetic acid, and acrolein) can be produced during the reaction, especially at lower temperatures (<650 °C), due to the complex reaction pathways of GSR. These by-products limit the overall efficiency of hydrogen production [21,22]. Therefore, a catalyst used in GSR should be capable of effectively converting glycerol into gaseous products, while inhibiting other hydrogen-consuming side-reactions, such as the hydrogenation of CO and CO<sub>2</sub> to methane and other hydrocarbons, as well as the reverse water-gas shift (RWGS) reaction [23-25]. Noble metals like Rh, Ir, and Pt are highly active in this regard but are not favored for industrial implementation due to their prohibitive costs [26,27]. Among the more affordable transition metals, Ni is often preferred (over e.g., Co or Cu), because of its ability to break down glycerol molecules via the C-C bond rupture [28,29]. However, Ni catalysts have drawbacks, including susceptibility to deactivation through carbon deposition and metal particle sintering, as well as high activity for COx methanation at lower temperatures [30,31].

Perovskite oxides have recently emerged as an important and versatile class of materials, with a wide range of potential applications as heterogeneous catalysts [32-34], including the steam reforming of glycerol [34,35]. They are also highly suitable as supports for Ni catalysts, as they inhibit catalyst deactivation and promote catalytic stability [36-38]. This has been documented for Ni/perovskite supported catalysts, where Ni was introduced via deposition or impregnation on an already preformed perovskite matrix [39-41], as well as for the so-called "exsolved" catalysts, where Ni was previously solubilized into the perovskite solid solution, occupying part of the B-sites in the lattice [42, 43]. During exsolution, a Ni-doped perovskite is reduced at high temperatures, which promotes the migration of Ni<sup>2+</sup> cations to the surface and the subsequent formation of small, uniform, well-dispersed, and partly submerged (socketed) Ni nanoparticles that exhibit a particularly strong metal-support interaction [33,44]. These exsolved nanoparticles have shown exceptional resistance to deactivation via sintering and

coking. Their socketed nature prevents displacement and excessive coke deposition on their surface, in stark contrast to similar impregnated Ni catalysts (e.g., Ni/Al $_2$ O $_3$  or Ni/ZrO $_2$ ) [17,24,38,42,44]. The smaller particle size and exposed metallic Ni surface induced via exsolution also help disfavor H-coverage and hydrogen consumption for the methanation of CO/CO $_2$  [37,43].

Until now, a certain number of studies have reported on the activity of Ni catalysts supported on perovskite oxides for the GSR reaction [14, 35,36,45-50]. For example, Wu et al. [45] and Aman et al. [46] showed that Ni/La<sub>2</sub>O<sub>3</sub> derived from the reductive decomposition of LaNiO<sub>3</sub> is highly active and stable for the GSR reaction. Wu et al. [45] additionally prepared Ca-doped LaNiO<sub>3</sub> and showed that Ca-doping can increase the catalytic stability, with the H2 yield dropping however from approx. 6 to 5 mol H<sub>2</sub> per mol of glycerol during 30 h of operation. Furthermore, other literature works showed that substitution of the LaNiO<sub>3</sub> perovskite with Ce [47] or Cu [48] further enhanced the catalytic activity and hindered deactivation through sintering and coke deposition. Particularly high catalytic stability during 24 h of operation was achieved in the case of Cu-substitution in the work of Ramesh et al. [48], who reported a rather stable glycerol conversion of approx. 72 % with an H<sub>2</sub> selectivity of approx. 68 %. On the other hand, modifying the LaNiO<sub>3</sub> preparation method by adding cellulose and EDTA was also found to reduce the Ni<sup>0</sup> particle size, thereby promoting catalytic activity and stability, with a stable approx. 70 % glycerol conversion and H2 selectivity during 24 h of operation [49]. Additionally, via impregnation, Ni catalysts introduced onto preformed perovskite-type supports, such as CeAlO<sub>3</sub> (or AlCeO<sub>3</sub>), also exhibited good GSR activity and stable time-on-stream performance [14,50]. It is however noted, that LaNiO<sub>3</sub>-derived catalysts have a high content of La and Ni (in the range of 25 wt% for Ni) and thus, the use of lower Ni loadings and support oxides with cheaper elements is preferred.

Although modifying GSR catalyst supports with alkaline earth metals (Mg, Ca, Sr, and Ba) has enhanced catalytic performance [25,51–54], incorporating these metals into perovskite oxides has been minimally investigated. Wu et al. [45] showed that 50 % Ca substitution in the A-site of LaNiO $_3$  could improve metal-support interaction and increase Ni dispersion. However, this approach resulted in incomplete formation of the precursor perovskite and significant coke deposition due to high Ni loading. Alkaline earth metal zirconate perovskites (i.e., CaZrO $_3$ , SrZrO $_3$  and BaZrO $_3$ ) employ cheaper elements (Ca, Sr, Ba and Zr) and have been effectively used in other reactions [55,56]. Specifically, Ni-doped CaZrO $_3$  has shown remarkable catalytic stability and coking resistance during 500 h of time-on-stream dry methane reforming at 800 °C, attributed to fine Ni dispersion, high oxygen mobility, and intimate metal-support interaction [56].

Prompted by the above, the present study takes inspiration from the exceptionally high catalytic activity and stability of Ni catalysts supported on CaZrO3, SrZrO3, and BaZrO3 perovskite oxides reported for other reactions, and employs these perovskite structures for the glycerol steam reforming (GSR) reaction, an approach that has not been investigated until now. Several characterization techniques, including XRD, N<sub>2</sub> physisorption, H<sub>2</sub>-TPR, H<sub>2</sub> pulse chemisorption, and CO<sub>2</sub>-TPD were carried out to examine the surface and bulk properties of the prepared catalysts and provide a thorough material characterization. Catalytic performance studies were carried out to determine the effect of the reaction temperature and time-on-stream on glycerol conversion and selectivity towards gaseous products, particularly H2, showing that the Ni catalyst supported on SrZrO<sub>3</sub> can provide a high performance with high H<sub>2</sub> selectivity and yield (>6 mol H<sub>2</sub>/mol of glycerol at 550 °C and above), as well as high stability during prolonged reaction operation under harsh reaction conditions. Finally, the spent catalysts that were characterized via Raman, TPO, and TEM/HAADF-STEM to study deactivation characteristics such as sintering and coking.

#### 2. Materials and methods

#### 2.1. Sample preparation

The perovskite materials were prepared by the solution autocombustion method. The following metal nitrates were added in calculated amounts:  $Sr(NO_3)_2$  (Aldrich, 99.995 %);  $Ba(NO_3)_2$  (Aldrich, 99.999 %);  $Ca(NO_3)_2 \cdot 4H_2O$  (Aldrich, 99.995 %);  $Ca(NO_3)_2 \cdot 6H_2O$  (Aldrich, 99.999 %). Glycine (NH<sub>2</sub>CH<sub>2</sub>COOH) was used as fuel with a molar ratio of  $\frac{NO_3^2}{Glycine} = 0.9$ ; all were dissolved in H<sub>2</sub>O. The temperature was gradually increased to ~250 °C to ignite the auto-combustion, with a rapid flame propagation that ended in a few minutes, producing very fine and voluminous powders that were then calcined at 800 °C or 950 °C (BaZ and BaZNi-7) for 5 h to remove carbonaceous impurities and form the corresponding perovskite crystalline phase. Ni was introduced during the autocombustion. The stoichiometry of the perovskite was not changed by reducing the Zr to introduce Ni, but the proper amount of Ni nitrate was introduced to have 7 wt%.

The solution auto-combustion method has been thus far employed for the synthesis of a wide range of materials [57]. The selection of an appropriate fuel nature and nitrate:fuel stoichiometric ratio are quite important since they can significantly influence the material's physicochemical properties and thus, its catalytic performance [57,58]. In this work, this particular synthesis method (solution auto-combustion), fuel (glycine), and nitrate:glycine ratio (0.9), were selected based on our prior works [59,60]. The use of a higher calcination temperature for BaZ and BaZNi-7 (950 °C) was employed in order to ensure the crystallization of the BaZrO<sub>3</sub> perovskite phase, since preliminary results (not shown here) revealed that 800 °C is insufficient to form the BaZrO<sub>3</sub> crystal structure. The prepared samples are listed in Table 1 below:

# 2.2. Sample characterization

Powder X-ray diffraction (XRD) patterns were collected using a SmartLab diffractometer (Rigaku) with Cu-K $\alpha$  radiation ( $\lambda=0.15418$  nm) in the range  $2\theta=10^{\circ}-90^{\circ}$  and scan rate  $0.3^{\circ}/min$ . The raw data were submitted on smoothing process by the Savitzky method, background elimination process by the Sonnevelt method, and  $K_{\alpha2}$  elimination process.

The nickel amount of the synthesized catalysts was obtained by Energy Dispersive X-ray Fluorescence (EDXRF) spectrometry using an EDX-720 (Shimadzu) instrument. N<sub>2</sub> adsorption/desorption isotherms were measured at  $-196\,^{\circ}\mathrm{C}$  using an ASAP 2020 (Micromeritics) adsorption apparatus. Degassing of the samples was carried out before analysis at 350  $^{\circ}\mathrm{C}$  under vacuum for 4 h. The specific surface area (SSA) was determined using the BET equation method in the linear relative pressure range (p/p<sup>0</sup>) of 0.07–0.3. Using the Barrett–Joyner–Halenda (BJH) method, the pore-size distributions were calculated from the desorption branches.

Temperature programmed reduction (H<sub>2</sub>-TPR) experiments were performed by a TPDRO1100 (Thermo Scientific) flow apparatus. The calcined sample (0.200 g) was placed into a quartz reactor and pre-

**Table 1**Sample names, calcination temperature, and Ni content.

Sample name	Stoichiometry	Calcination temperature (°C)	Ni content (wt %) <sup>a</sup>
BaZ	$BaZrO_3$	950	n.a.
CaZ	$CaZrO_3$	800	n.a.
SrZ	$SrZrO_3$	800	n.a.
BaZ-Ni7	Ni/BaZrO <sub>3</sub>	950	6.9
CaZ-Ni7	Ni/CaZrO <sub>3</sub>	800	7.2
SrZ-Ni7	Ni/SrZrO <sub>3</sub>	800	9.3

<sup>&</sup>lt;sup>a</sup> Ni content obtained by Energy Dispersive X-ray Fluorescence.

treated, flowing 20 cm³ min $^{-1}$  of 5 %  $\rm O_2/He$  gas mixture at 500 °C for 1 h and then cooled to 50 °C. Then, 30 cm³ min $^{-1}$  of 5 %  $\rm H_2/Ar$  gas mixture was fed into the reactor, and the temperature was raised to 800 °C, with a heating rate of 10 °C/min, holding at 800 °C for 1 h. The sample was then degassed at 850 °C, flowing 30 cm³ min $^{-1}$  of Ar, and then cooled down to 50 °C.

 $H_2$  **chemisorption** was subsequently performed using Ar as carrier gas at 30  ${\rm cm}^3~{\rm min}^{-1}$ , and the successive doses of 5 %  $H_2/{\rm Ar}$  gas mixture were subsequently introduced using a calibrated injection valve up to saturation. The  $H_2$  consumption/chemisorption was measured by a TCD detector and calibrated by reducing a known amount of CuO (99.99 % purity from Sigma Aldrich). The  $H_2{\rm O}$  generated in the reduction was removed by a trap before flowing into the TCD detector.

Temperature-programmed desorption of CO<sub>2</sub> (CO<sub>2</sub>-TPD): CO<sub>2</sub>-TPD experiments were carried out on Autosorb IQ/Quantachrome, in order to study the surface basicity of the catalytic materials. In a typical experiment, 0.1g of already reduced catalyst was placed in a U-shaped cell and was in-situ reduced again with 10.5 %  $\rm H_2/N_2$  mixture (50 mL min<sup>-1</sup>) for 30 min. Afterward, the system was cooled down to 25 °C under a flow of He (50 mL min<sup>-1</sup>) and a feed containing 10 % CO<sub>2</sub>/Ar was passed (50 mL min<sup>-1</sup>) through the catalyst for 30min. The physically adsorbed CO<sub>2</sub> was then removed by flowing He followed by the start of temperature raising up to 800 °C with a heating rate of 10 °C min<sup>-1</sup> to achieve the desorption and measurement of CO<sub>2</sub> via a TCD detector.

Raman spectra were collected using a Witec Alpha 300 RAS with a  $20 \times long$  distance objective (0.35 numerical aperture) in the back-scattering geometry with an excitation wavelength of 532 nm from an  $Ar^+$  ion laser.

Temperature-programmed oxidation (TPO) was performed in an oxidative atmosphere in order to determine the nature of carbonaceous deposits on the spent catalysts using the Micromeritics AutoChem II. Firstly, the spent catalyst was initially pretreated in the presence of highpurity He for 15 min, then cooled to room temperature. TPO experiment covered a temperature range of 40–800 °C under a mixture of 20 %  $O_2$ / He (Ramp = 10 °C/min). Upon reaching the target temperature, the recording by TCD detector ceased, and the system was cooled under a flow of He using a cooling rate of 20 °C/min.

**Transmission electron microscopy (TEM)** was performed on a T20 microscope (FEI-Tecnai, 200 kV) with a LaB<sub>6</sub> electron source and objective lens "SuperTwin®" that allows 0.24 nm point-to-point resolution. High-angle annular dark-field scanning transmission electron microscopy (HAADF-STEM) was performed with a field emission gun microscope (Analytical XFEG FEI Titan, 300 kV) equipped with Cs-probe allowing 0.09 nm mean size electron probe formation (CEOS).

#### 2.3. Catalytic testing

The experimental apparatus where the work was carried out has been described in detail in previous publications on the topic by our group [12,23]. Briefly, the experiments were carried out at atmospheric pressure on a continuous flow fixed-bed reactor with an internal diameter (ID) of 14 mm (Autoclave Engineers, BTRS Catalyst testing system). The system comprised vaporizers and a pre-heater (set at 350 °C, so that glycerol would be in the gas phase) before the reactor and a condenser afterward. The glycerol used had a purity of 99.5 % (Sigma Aldrich), and the glycerol/water mixture was fed to the system using an HPLC pump. The gaseous products were analyzed online using a gas chromatograph (Agilent 7890A) equipped with TCD and FID detectors. The liquid products were analyzed using a combination of Gas Chromatography (Agilent 7890A, FID detector) and Mass Spectroscopy (Agilent 5975C).

Catalyst activation was performed in situ, using high purity  $H_2$  (N5.0), at 800  $^{\circ}C$  for 1 h (100 ml min $^{-1}$ ) and a catalyst weight of 200 mg in powder form (dp < 56  $\mu m$ ).

Two different experimental protocols were used for the work carried out herein.

The first experimental protocol assessed the catalytic activity and selectivity between 400 and 750 °C (50 °C steps, where 50 min were spent at each step to ensure steady-state conditions). For gas products, each measurement was obtained thrice, helping to ensure the reproducibility of the results. Liquid products were obtained once at every temperature step (i.e., at the end of the 50 min period). The liquid feed (0.12 mL min $^{-1}$ ) consisted of 20 %  $\rm C_3H_8O_3$  diluted in  $\rm H_2O$ . The gas feed was He, at a Weight Hourly Space Velocity (WHSV) equal to 50,000 mL g $^{-1}$  h $^{-1}$ . Thus, the gas feed at the reactor's inlet consisted of a gas mixture of 73 %  $\rm H_2O$ , 4 %  $\rm C_3H_8O_3$ , and 23 % He.

The second experimental protocol examined catalytic stability during time-on-stream experiments. The work was carried out at 600  $^{\circ}\text{C}$ , under more severe conditions (i.e., 63 %  $H_2\text{O}$ , 7 %  $C_3H_8\text{O}_3$ , 30 % He, WHSV = 50,000 mL g $^{-1}$  h $^{-1}$ ), to provoke catalyst deactivation. Gaseous products were measured hourly, and liquid products every 5 h. Catalytic stability was assessed over a 20 h period.

#### 2.4. Reaction metrics

Glycerol conversion is calculated based on the mols of glycerol at the reactor inlet and outlet. The catalytic performance in the gas phase is reported in terms of H<sub>2</sub> yield, H<sub>2</sub>, CO, CH<sub>4</sub>, and CO<sub>2</sub> selectivity, glycerol conversion into gaseous products, and total glycerol conversion, and in the liquid phase in terms of acetol, acetone, allyl alcohol, acetaldehyde, acrolein, and acetic acid selectivity. The following equations were used:

$$\% glycerolconversion_{(globalconversion)} = \left(\frac{Glycerol_{in} - Glycerol_{out}}{Glycerol_{in}}\right) \times 100$$
 (4)

$$\% glycerol conversion_{(gaseous products)} = \left(\frac{Catoms in the gas products}{total Catoms in the feed stock}\right) \times 100 \tag{5}$$

$$H_2 yield = \frac{H_2 moles produced}{moles of glycerol in the feeds tock}$$
 (6)

$$\% H_2 selectivity = \left(\frac{H_2 mole sproduced}{Catoms produced in the gas phase}\right) \times \left(\frac{1}{RR}\right) \times 100 \tag{7}$$

where, RR is the reforming ratio (7/3), defined as the ratio of moles of  $\rm H_2$  to  $\rm CO_2$  formed.

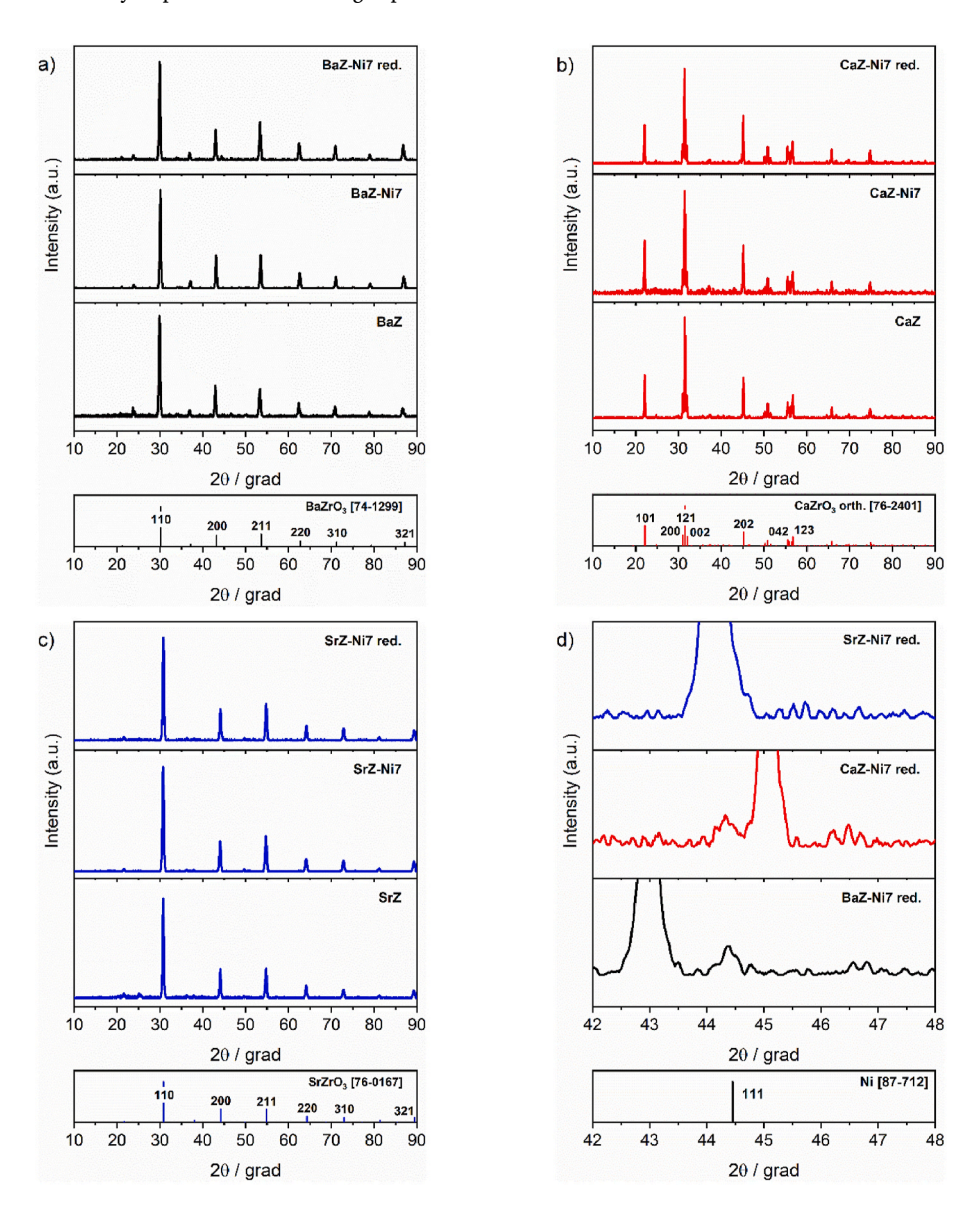


Fig. 1. X-ray diffraction patterns of the calcined MeZ perovskite supports, and the calcined/reduced MeZ-Ni7 catalysts: (a) BaZ and BaZ-Ni7; (b) CaZ and CaZ-Ni7; (c) SrZ and SrZ-Ni7, and (d) Patterns in the range of  $2\theta = 42-48^{\circ}$  showing the Ni<sup>0</sup> (111) peak for the reduced MeZ-Ni7 catalysts.

$$\% selectivity of i = \left(\frac{Catoms in species i}{Catoms produced in the gasphase}\right) \times 100 \tag{8}$$

where, species i refers to CO, CO<sub>2</sub>, and CH<sub>4</sub>.

$$\% selectivity of i' = \left(\frac{\textit{Catomsinspeciesi'}}{\textit{Catomsproduced in the liquid phase}}\right) \times 100 \tag{9}$$

where, species i' refers to acetol, acetone, allyl alcohol, acetaldehyde, acrolein, and acetic acid.

#### 3. Results and discussion

#### 3.1. Catalyst characterization

#### 3.1.1. XRD characterization

XRD analysis was performed on the MeZ (Me = Ba, Ca, Sr) supports and the MeZ-Ni7 catalysts, both calcined and after reduction to 800  $^{\circ}$ C, and the results are shown in Fig. 1.

BaZ and SrZ predominantly constituted of the perovskite phase with a cubic crystalline structure belonging to the *Pm3-m* space group. On the contrary, CaZ formed a perovskite phase with orthorhombic structure and *Pcmn* space group. The main peak of the perovskite was at 29.9°,  $30.7^{\circ}$ , and  $31.5^{\circ}$  20 for BaZ, SrZ, and CaZ, according to the ionic radius of the alkaline earth element that is 1.61, 1.44, and 1.34 Å for Ba<sup>2+</sup>, Sr<sup>2+</sup>, and Ca<sup>2+</sup> in 12-coordination, respectively. In addition to the perovskite phase, other reflections appeared on the BaZ sample attributed to BaCO<sub>3</sub>, whereas only trace amounts of SrCO<sub>3</sub> remained after calcination on SrZ. The Goldshmidt tolerance factor t [61] for the perovskite structure was calculated by the following equation, in which  $r_{Me}$  is the ionic radius of the alkaline earth element,  $r_{Zr}$  is the ionic radius of Zr<sup>4+</sup> = 0.72 Å, and  $r_O$  is the ionic radius of  $O^{2-} = 1.35$  Å.

$$t = \frac{r_{Me} + r_O}{\sqrt{2}(r_{Zr} + r_O)} \tag{10}$$

The t values were 0.96, 0.90, and 0.87 for BaZ, SrZ, and CaZ, respectively. A cubic perovskite is predicted for t values in the range 0.90–1.00, and lower symmetry structures are formed for t values in the range 0.70–0.90 [62,63], confirming the results of the XRD analysis. Thus, BaZ and SrZ have ideal sizes for cubic systems belonging to the Pm-3m space group; on the other hand, CaZ shows an orthorhombic structure, belonging to the Pcmn space group.

Moreover, for BaZ, the presence of other impurities phases can be caused by the calcination temperature of 950  $^{\circ}$ C that, although significantly higher than that used for the other samples, still does not induce the full perovskite formation.

The diffractograms of the calcined Ni-containing samples did not show the peaks ascribed to cubic NiO, indicating that NiO was amorphous or that part of Ni<sup>2+</sup> was in a solid solution with the perovskite [37]. However, the fraction in the solid solution is difficult to clarify; the main peak of the perovskite, i.e.,  $30.1^{\circ}$ ,  $30.7^{\circ}$  and  $31.4^{\circ}$   $2\theta$  for BaZ-Ni7, SrZ-Ni7 and CaZ-Ni7, did not show substantial displacement with respect to the MeZ perovskite supports (Me = Ba, Ca, Sr).

After reduction at 800 °C, the perovskite phase remained unchanged. Furthermore, as shown in Fig. 1, BaZ-Ni7 and CaZ-Ni7 showed a weak peak at 44.4° 20 due to the (111) reflection of metallic Ni<sup>0</sup>. However, in SrZ-Ni7, this peak was not revealed, and it was superimposed by the more intense (200) reflection of the SrZrO<sub>3</sub> support. The average size of the Ni<sup>0</sup> crystallites was obtained by the X-ray line broadening method [64] using the Scherrer equation where D is the crystallite size of Ni<sup>0</sup> in nm, K is the crystallite-shape factor assumed as 0.9;  $\lambda$  is the wavelength of the Cu-K $_{\alpha}$  radiation (0.15418 nm),  $\beta_{D}$  is the full-width at half maximum in radians, due to the crystallites size effect, and  $\theta$  is the Bragg angle.

$$D = \frac{K\lambda}{\beta_D \cdot \cos \theta} \tag{11}$$

The calculations were possible only for the detectable (111) peak of  $\mathrm{Ni}^0$ , in CaZ-Ni7 and BaZ-Ni7. As reported in Table 2, the  $\mathrm{Ni}^0$  crystallite size was similar, 24.8 nm and 29.8 nm for CaZ-Ni7 and BaZ-Ni7, respectively.

The Williamson Hall method [65] was used to obtain the crystallites size of the perovskites. By neglecting the instrumental broadening, the full width at half maximum  $\beta_T$  of every diffraction peak is ascribed to the broadening effect of both the crystallite size  $\beta_D$  and the lattice strain arising from imperfection and distortion of the crystallites  $\beta_s$ , according to the following equations:

$$\beta_T = \beta_D + \beta_s \tag{12}$$

$$\beta_s = 4\varepsilon \tan \theta \tag{13}$$

in Eq. (13)  $\varepsilon$  is the strain-induced broadening.

Then, rearranging Eqs. (11)–(13) we get the uniform deformation model (UDF) [66], according to Eq. (14):

$$\beta_T \cdot \cos \theta = \frac{K\lambda}{D} + 4\varepsilon \cdot \sin \theta \tag{14}$$

By plotting the  $\beta_T \cdot \cos \theta$  with respect to  $4 \cdot \sin \theta$ , we obtained the Williamson Hall plot shown in Fig. 2. From the intercept with the y-axis, it was possible to calculate the crystallite size D, while the slope of the fitting line was the strain-induced broadening  $\varepsilon$ .

The dimensions of the crystallites followed the order BaZ < SrZ < CaZ. BaZ showed the smallest crystallites despite having been obtained at a higher calcination temperature due to the more difficult formation of the pure perovskite phase.

The strain-induced broadening  $\varepsilon$  followed the order CaZ < SrZ < BaZ, different from the crystallite size trend, indicating that the imperfections and distortion of the crystals were limited mainly in the CaZ perovskite.

The introduction of Ni significantly changed the crystallite size of the perovskite, which, although in the same order, decreased by about 50 % for CaZ-Ni7 and SrZ-Ni7 samples, while it showed a minor decrease of 9 % in BaZ-Ni7. The strain-induced broadening, $\varepsilon$ , diminished significantly, becoming negligible.

After the reduction at 800  $^{\circ}$ C, the crystallite size of the perovskite did not increase, indicating the absence of sintering. The strain-induced broadening remained low, or practically zero in the case of SrZ-Ni7. For the CaZ-Ni7 sample, although low, the negative value was due to the lattice shrinkage [66] originated by oxygen vacancy formation during the reduction treatment at high temperatures.

# 3.1.2. Textural characterization

The  $N_2$  physisorption isotherms of the MeZ perovskite supports and the MeZ-Ni7 catalysts are reported in Fig. 3, while the corresponding textural properties are summarized in Table 3.

Table 2  $D_{W\text{-}H\text{-}}\,\,\epsilon,\,\text{and}\,\,D^0_{Ni}\,\text{for the supports and calcined and reduced catalysts}.$ 

Sample	D <sub>W-H</sub> (nm) <sup>a</sup>	$\epsilon\times10^3$	$D_{Ni^0}$ (nm) <sup>b</sup>
BaZ	31.1	1.20	n.a.
BaZ-Ni7	28.4	0.55	n.a.
BaZ-Ni7 red.	27.7	0.61	29.8
CaZ	70.4	0.82	n.a.
CaZ-Ni7	35.9	0.37	n.a.
CaZ-Ni7 red.	34.6	-0.32	24.8
SrZ	45.3	1.42	n.a.
SrZ-Ni7	24.8	0.53	n.a.
SrZ-Ni7 red.	24.9	0.07	n.a.

<sup>&</sup>lt;sup>a</sup> Calculated by the Williamson-Hall plot method.

<sup>&</sup>lt;sup>b</sup> Calculated by the Scherrer equation of the (111) peak of Ni.<sup>0</sup>.

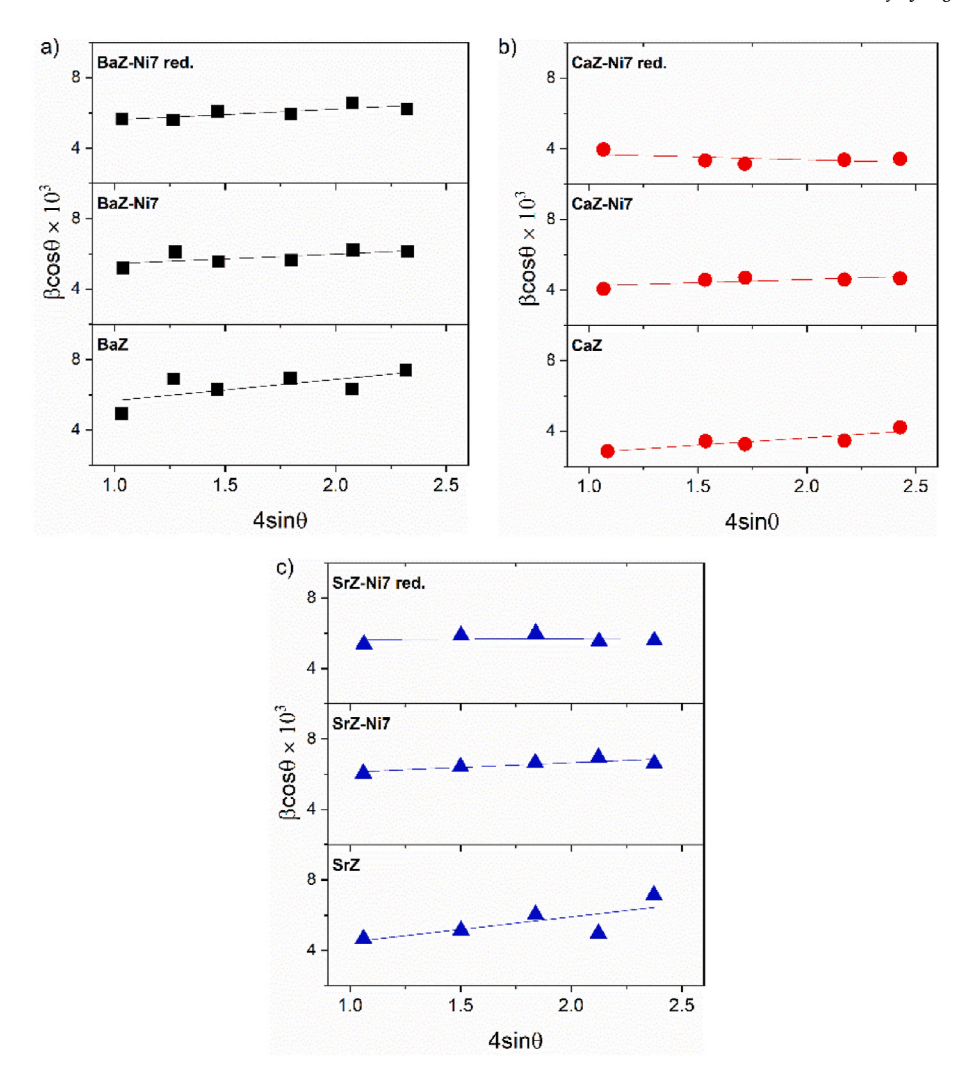


Fig. 2. Williamson-Hall plots of the calcined MeZ perovskite supports, and the calcined and reduced MeZ-Ni7 catalysts: (a) BaZ and BaZ-Ni7; (b) CaZ and CaZ-Ni7; and, (c) SrZ and SrZ-Ni7.

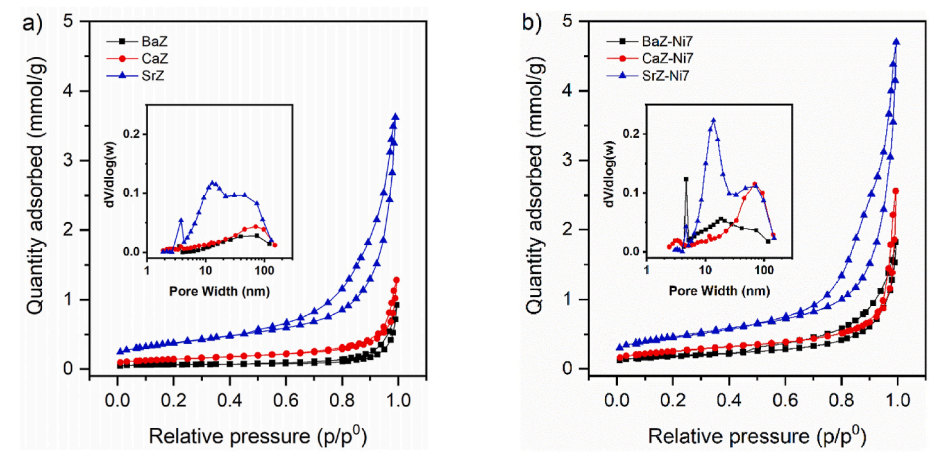


Fig. 3. N<sub>2</sub> adsorption-desorption isotherms and pore size distributions (inset) of the MeZ perovskite supports (a) and MeZ-Ni7 catalysts (b).

According to the IUPAC [67] recommendations, the  $N_2$  physisorption isotherms of BaZ and CaZ perovskites have been classified as Type II, associated with non-porous or macroporous adsorbents, with a small H3 hysteresis loop, related to macro-pores that are not filled with pore condensate. Meanwhile, the SrZ perovskite showed pseudo-Type II

isotherms, with an H3 hysteresis loop observed mainly in aggregates of plate-like particles. The BJH pore size distributions were obtained from the desorption branches, and the presence of macro-pores was undoubtedly observed on the BaZ and CaZ samples; however, a distinct pore size distribution in the meso-pores range, with the maximums at

**Table 3**Textural properties of the as-prepared MeZ perovskite supports and MeZ-Ni7 catalysts.

Sample	SSA $(m^2g^{-1})$	Pore Volume (cm <sup>3</sup> g <sup>-1</sup> )
BaZ	5	0.03
CaZ	11	0.04
SrZ	30	0.12
BaZ-Ni7	14	0.07
CaZ-Ni7	20	0.09
SrZ-Ni7	37	0.17

#### 3.7 and 13.6 nm, appeared on SrZ.

The introduction of Ni significantly changed the textural properties of the calcined MeZ-Ni7 catalysts. BaZ-Ni7 was characterized by pseudo-Type II isotherms, with a pronounced H3 hysteresis loop that closed at around 0.45 p/p<sup>0</sup>, indicating the presence of mesopores. In fact, the BJH pore size distribution of BaZ-Ni7 showed a sharp peak at 4.7 nm and a broad one at 18.7 nm. CaZ-Ni7 maintained the same N<sub>2</sub> physisorption behavior of the bare CaZ perovskite support, with a Type II isotherm having a small H3 hysteresis loop due to the presence of macro-pores but with a considerably higher quantity of N<sub>2</sub> physisorbed in the wall p/p<sup>0</sup> range. The isotherms of SrZ-Ni7 catalyst were classifiable as pseudo-Type II with an intermediate trend between the H1 and H2 hysteresis loops. As evidenced by the BJH pore size distribution, much of the physisorbed N<sub>2</sub> was distributed on the pores with 13.6 nm in size.

As detailed in Tables 3 and it is clear that Sr allowed the formation of perovskites with the highest surface area and pore volume, and that the addition of nickel further increased the surface area of the perovskites, regardless of the alkaline earth metal in the A-site.

#### 3.1.3. H<sub>2</sub>-TPR and H<sub>2</sub>-pulse characterization

Catalyst reducibility was studied by hydrogen temperature-programmed reduction ( $H_2$ -TPR) and Ni dispersion by dynamic hydrogen chemisorption measurements ( $H_2$ -pulse chemisorption). The reduction profiles of the perovskite supports are presented in Fig. 4a. BaZ revealed a weak peak that started at 700 °C and did not end until 800 °C. SrZ showed three peaks with increasing intensity at 460, 580, and 680 °C superimposed on a further strong peak, which, also in this case, did not end up at 800 °C. Finally, the CaZ reduction profile was characterized by an intense and broad peak at 650 °C.

The reduction of MeCO $_3$  (Me = Ba, Ca, Sr) impurities (Equation (15)) [68] was excluded because they were removed by the O $_2$ /He pretreatment. Furthermore, in the H $_2$ -TPR experiment, alkaline earth ions Me $^{2+}$  retain their oxidation state, while transition metal Zr $^{4+}$  is partially reduced to Zr $^{3+}$  [69,70]. H $_2$  consumption due to the oxygen vacancy formation [70,71] on the perovskite surface or lattice can also be detected, according to Equation (16) (as evidenced by the slight color

change of the reduced samples). The  $\rm H_2$  consumption of the MeZ perovskite supports, reported in Table 4, decreased significantly following the order  $\rm SrZ > CaZ > BaZ$ , a trend partly correlated to the tolerance factor t of the perovskite specimen.

$$MeCO_3 + 4H_2 \rightarrow MeO + CH_4 + 2H_2O$$
 (15)

$$O_0 + H_2 \rightarrow H_2O + V_0^- + 2e^-$$
 (16)

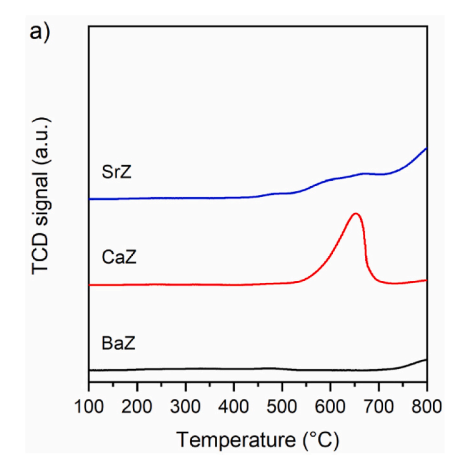
The reduction profiles of the Ni-perovskite catalysts are shown in Fig. 4b. BaZ-Ni7 showed two very weak peaks at 186 and 274 °C, attributed to amorphous NiO barely interacting with the support [60]. In the temperature range of 300-725 °C, three strong and superimposed peaks ( $\alpha$ ,  $\beta$  and  $\gamma$ ) were revealed. The  $\alpha$  (400–443 °C) and  $\beta$  (530–560 °C) peaks were found in BaZ-Ni7 and CaZ-Ni7, whereas the y peak (620-640 °C) was observed in CaZ-Ni7 and SrZ-Ni7. They were ascribed to the reduction of Ni<sup>2+</sup> species in different interactions with the perovskite [60] and oxygen vacancy formation, as highlighted above. The  $\alpha$  and  $\beta$  species corresponded to NiO in the surface and sub-surface of the perovskites, respectively, interacting strongly with the perovskite support. The  $\gamma$  species can be attributed to Ni<sup>2+</sup> solubilization into the perovskite structure, thus making it more difficult to reduce. Therefore, the  $\gamma$ -peak most probably occurs upon exsolution of the  $\mathrm{Ni}^{2+}$  ions onto the perovskite surface, a process which is known to result in well-dispersed and socketed nanoparticles in very strong interaction with their underlying support [72-74].

On BaZ-Ni7 and CaZ-Ni7 samples, the small, broad and weak reduction peak at higher temperatures indicated the formation of oxygen vacancies in the lattice [69]. However, the interaction of Ni<sup>2+</sup> species with the surface and the bulk makes a direct correlation with the reduction of the perovskite support more arduous [71,73]. Anyhow, the hydrogen consumption of the MeZ-Ni7 catalysts reported in Table 4 was in line with a complete  $Ni^{2+} \rightarrow Ni^{0}$  reduction.

The Ni surface area per gram of Ni  $(S_{Ni})$  was obtained from the pulse

**Table 4** Quantitative results obtained by the temperature-programmed reduction and the  $H_2$  pulse chemisorption techniques.  $H_2$  consumption, Ni surface area per gram of Ni  $(S_{Ni})$ , Ni metal dispersion  $(D_{Ni})$  and Ni aggregate size  $(d_{Ni})$ .

Sample	$H_2$ consumption ( $10^3 \times mol \ g^{-1}$ )	$S_{Ni}\;(m^2g_{Ni}^{-1})$	$D_{Ni}$ (%)	$d_{Ni}$ (nm)
BaZ	0.08	n.a.	n.a.	n.a.
CaZ	0.34	n.a.	n.a.	n.a.
SrZ	0.54	n.a.	n.a.	n.a.
BaZ-Ni7	1.24	23.5	3.6	28.6
CaZ-	1.36	8.6	1.3	78.1
Ni7				
SrZ-Ni7	1.42	4.8	0.7	140.4



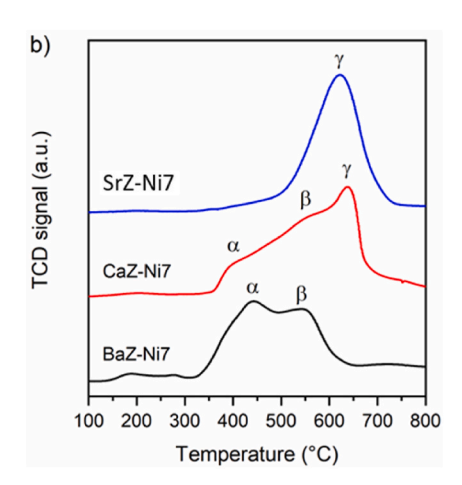


Fig. 4. H<sub>2</sub>-TPR profiles of: (a) MeZ perovskite supports, and (b) MeZ-Ni7 catalysts.

chemisorption of H<sub>2</sub> using the following formula:

$$S_{Ni} = \frac{U}{vW} N_A \sigma \tag{17}$$

where U is the amount of  $H_2$  adsorbed (mol);  $\nu$  is the adsorption stoichiometric factor, W is the amount of metal (Ni, in g);  $N_A$  is the Avogadro number;  $\sigma$  is the atomic surface area.

The Ni metal dispersion  $(D_{Ni})$  was calculated using the following equation

$$D_{Ni} = A \times \frac{U}{vW} \tag{18}$$

where A is the metal atomic weight. Further information about Equations (17) and (18) is contained in Ref. [74]. The H<sub>2</sub>-pulse profiles can be found in Fig. S1, at the Supplementary Material.

The Ni aggregate size  $(d_{Ni})$  was estimated assuming spherical shape for the Ni particles, using the following formula, where  $\rho$  represents the metal density.

$$d_{Ni} = \frac{6}{S_{Ni}\rho} \tag{19}$$

The BaZ-Ni7 catalyst showed the highest  $S_{Ni}$ ,  $D_{Ni}$  and  $d_{Ni}$  values, while they decreased significantly for the other catalysts. These results, however, were not correlated with the Ni<sup>0</sup> crystallite size obtained by XRD analysis of BaZ-Ni7 and CaZ-Ni7 catalysts (Scherrer equation), which, conversely, showed very similar dimensions. It is hypothesized that this apparent anomaly is due to the different interactions between Ni<sup>0</sup> and the perovskite, which influenced the H<sub>2</sub> chemisorption. Hence, Ni was reduced in CaZ-Ni7 and SrZ-Ni7 catalysts but continued interacting with the perovskite, probably becoming partially positively polarized  $Ni^{\delta+}$  and, thus preventing full H<sub>2</sub> chemisorption on the metal particle surface [75]. The interaction was more significant in the Ca-based and Sr-based perovskites. This hypothesis may also correlate with the lower formation of carbon residues observed after the catalytic test for spent CaZNi-7 and spent SrZNi-7.

# 3.1.4. Basic properties (CO<sub>2</sub>-TPD)

 ${
m CO_2}$ -TPD experiments (Fig. 5) were conducted for all catalytic samples (following pre-treatment in a hydrogen atmosphere) to investigate the nature and strength of the surface basic sites. The surface basicity can be divided into three regions based on the  ${
m CO_2}$  desorption temperature, which corresponds to three types of basic sites with varying strengths.  ${
m CO_2}$  desorption peaks below 250 °C, between 250 and 500 °C,

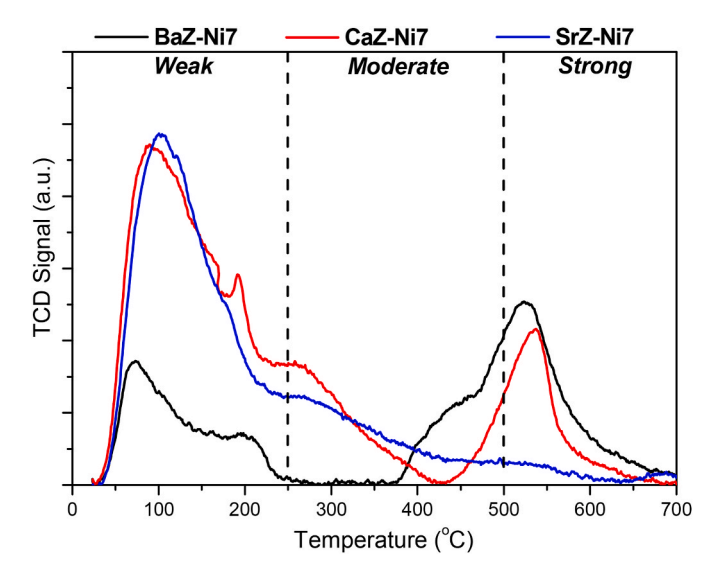


Fig. 5. CO<sub>2</sub>-TPD profiles of the MeZ-Ni7 catalysts.

and above 500 °C, can be attributed to basic sites of weak, moderate, and high strength, respectively [14,20]. As can be observed in Fig. 5, the population of moderately-strong basic sites in all samples is rather limited. Moreover, it appears that the presence of  ${\rm Ca}^{2+}$  or  ${\rm Sr}^{2+}$  in the perovskite A-site, instead of  ${\rm Ba}^{2+}$ , can provide an increased population of weak basic sites for CaZNi-7 and SrZNi-7. It can also be observed that the CaZ-Ni7 catalyst, like BaZNi-7, possesses a high population of basic sites with high strength. According to the literature [76], the increased population of basic sites enhances the rate of water adsorption and dissociation on the catalyst surface, generating hydroxyl ions (OH $^-$ ) that interact with glycerol. This activation step is essential in breaking down glycerol's C–C and C–O bonds, which promotes the reforming reaction and enhances the production of H $_2$ . Finally, the surface basic sites can increase the catalytic performance by adsorbing the CO $_2$  product, which shifts the reaction equilibrium towards greater H $_2$  production.

#### 3.2. Evaluation of the catalytic performance

# 3.2.1. Influence of supports

The influence of reaction temperature on the total glycerol conversion (X<sub>C3H8O3</sub>, %) along with glycerol conversion to gaseous products (X<sub>C3H8O3</sub> gaseous, %), on hydrogen selectivity (S<sub>H2</sub>) and yield (Y<sub>H2</sub>), as well as on the molar ratios of H<sub>2</sub>/CO and CO/CO<sub>2</sub> for the bare perovskite supports is presented in Fig. 6a-c. The influence of temperature on the liquid product selectivity for the supports is depicted in Fig. 6d-f. It has previously been demonstrated that glycerol decomposition can involve thermal cracking reactions without contact with the catalyst and the acid-base catalyzed reactions at the acidic and basic sites of the catalyst support [17,22,23]. As the overall process is endothermic, increasing temperatures leads to a strong increase in the conversion of glycerol [23]. The activity of the bare perovskite supports appears similar, except for a slightly higher overall glycerol conversion and conversion towards gaseous products for CaZ and SrZ. The catalytic activity of the bare perovskite supports rather resembles that of mesoporous Al<sub>2</sub>O<sub>3</sub>, and is only slightly improved compared to the empty reactor [23-25]. The small improvement compared to the thermal conversion can be attributed to the surface population of defect sites that are conducive to the surface activation of steam and gaseous glycerol [20]. CaZ and SrZ, with a lower tolerance factor than BaZ, can offer more of these sites. In addition, the contribution of some segregated alkaline earth oxide or carbonate phases (MeO and MeCO<sub>3</sub>) should also be considered.

The impact of reaction temperature on the  $\rm H_2/CO$  and  $\rm CO/CO_2$  molar ratios in the gaseous products for the bare perovskite supports is presented in Fig. 6c. The  $\rm CO/CO_2$  molar ratio increases with temperature, peaking at 600–650 °C, before decreasing up to 750 °C. The observed CO production at lower temperatures may result from glycerol decomposition, while the increase up to 650 °C is likely enhanced by the reverse water–gas shift reaction (RWGS). On the other hand, the  $\rm H_2/CO$  molar ratio exhibits the opposite trend, decreasing up to 600–650 °C, and then rising as the temperature continues to increase. Among the samples, the SrZ support demonstrates a significantly higher  $\rm H_2/CO$  ratio compared to CaZ and BaZ, at temperatures higher than 650 °C.

## 3.2.2. Ni catalysts

The influence of reaction temperature on the catalytic activity and product selectivity for the Ni-supported catalysts, and the homogeneous reaction, is depicted in Fig. 7a-h, and, as can be observed, there is a clear divergence from the thermal conversion of glycerol and the catalytic activity of the bare perovskite supports. The differences include a higher total conversion of glycerol, especially conversion towards gaseous products, a considerably higher  $\rm H_2$  production, an improved  $\rm H_2/CO$  ratio at the temperature range of 500–700 °C, and a total change in the liquid products' distribution, which are eliminated for the CaZ-Ni7 and SrZ-Ni7 catalysts above the temperature of 500 °C. This can be ascribed to the high activity of the catalytically active metallic Ni phase in synergy and in strong interaction with the underlying perovskite support,

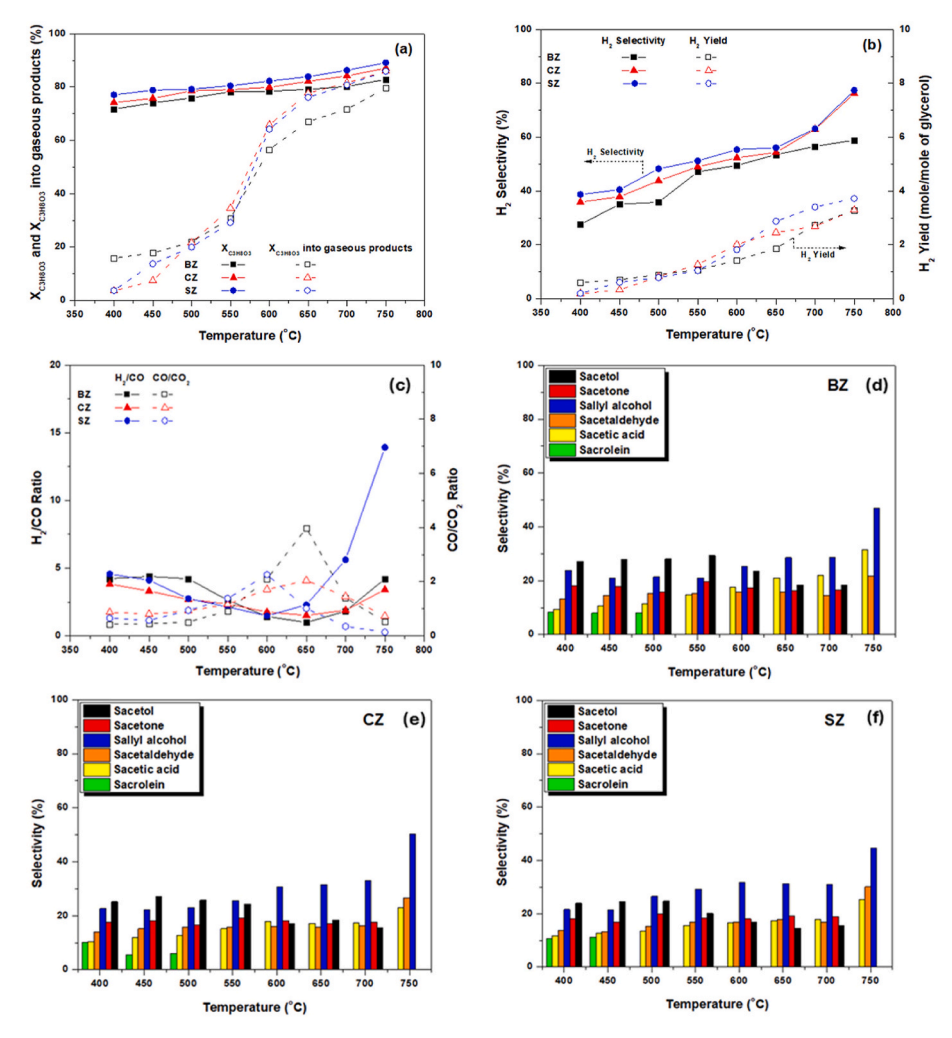


Fig. 6. (a) Total glycerol conversion and glycerol conversion into gaseous products, (b)  $H_2$  selectivity and yield, (c)  $H_2$ /CO and CO/CO<sub>2</sub> molar ratios, and (d-f) liquid products selectivity for the MeZ perovskite oxide supports used herein, (d) BZ, (e) CZ, and (f) SZ. [Results obtained for samples tested under the reaction conditions:  $C_3H_8O_3$  (20 wt %)/ $H_2O$  (total liquid flow rate = 0.12 mL min<sup>-1</sup>)/He = 38 mL min<sup>-1</sup>, WHSV = 50,000 mL g<sup>-1</sup> h<sup>-1</sup>,  $w_{catalyst}$  = 200 mg, T = 400–750 °C].

being able to effectively split C–C, C–O, and C–H bonds in glycerol, and release gaseous  $H_2$  and  $CO_x$  [20,25,47].

When comparing the three different catalysts (BaZ-Ni7, CaZ-Ni7, and SrZ-Ni7), it can be observed that BaZ-Ni7 exhibits the worst catalytic activity regarding glycerol conversion and H2 production. At the same time, CaZ-Ni7 and especially SrZ-Ni7 can more effectively convert glycerol into gaseous products, particularly H2. This can be ascribed to the higher Ni dispersion, increased availability of active sites for the dissociation of C<sub>3</sub>H<sub>8</sub>O and H<sub>2</sub>O molecules, and a more favorable and stronger Ni-support interaction, as the Ni exsolution process is more prominent on CaZ-Ni7 and SrZ-Ni7. The beneficial catalyst properties of CaZ-Ni7 and SrZ-Ni7 can effectively eliminate all liquid products (acetol, acetone, allyl alcohol, acetaldehyde, and acetic acid) at temperatures higher than 500 °C, converting the entirety of glycerol to gaseous products. Selectivity for CH<sub>4</sub> (carbon basis), which can arise from CO<sub>x</sub> hydrogenation, is also limited to below 10 % for the CaZ-Ni7 and SrZ-Ni7 catalysts (Fig. 8d). CO selectivity also lies at below 20 % for temperatures higher than 500 °C (not shown herein), meaning that the reverse water-gas shift reaction (RWGS), which consumes H2 to generate CO, is disfavored [77].

It is important to note herein that, for the BaZ-Ni7 sample, CH<sub>4</sub> selectivity remains minimal at lower reaction temperatures (400–550 °C) but increases significantly as the temperature rises, reaching a maximum value of approximately 17 % at 750 °C. In contrast, for the CaZ-Ni7 and SrZ-Ni7 samples, CH<sub>4</sub> selectivity shows a slight

increase at lower reaction temperatures (450–500 °C), while it decreases at higher temperatures, with the SrZ-Ni7 catalyst exhibiting the lowest CH<sub>4</sub> selectivity value, approximately 1.5 %. These findings are consistent with previous studies, which have shown that at high reaction temperatures (>600 °C) and under conditions with an increased water-to-glycerol feed ratio, as in this study, CH<sub>4</sub> formation is inhibited, promoting H<sub>2</sub> production through the methane steam reforming side-reaction.

Therefore,  $\rm H_2$  and  $\rm CO_2$  account for the majority of the reaction products generated via the CaZ-Ni7 and SrZ-Ni7 catalysts, which is well-suited for maximizing  $\rm H_2$  production [25]. SrZ-Ni7 is a better choice, as it offers higher  $\rm H_2$  productivity. The  $\rm H_2/CO$  ratio peaks for this catalyst at above 30 for 550 °C temperature, meaning that the produced gas could be directly fed into fuel cell stacks, without the need for extensive downstream processing and purification [78].

Finally, as illustrated in Fig. 7, in the absence of catalyst (empty reactor), glycerol conversion values exceeded 40 % at temperatures below 600 °C. At higher temperatures, an increase in total glycerol conversion was observed (Fig. 7a), leading to the production of gaseous products, such as  $\rm H_2$ , CO, CO<sub>2</sub>, and CH<sub>4</sub>. Over the entire temperature range of the reaction, the main liquid products are presented in Fig. 7h. Within the temperature range of 400–600 °C, the primary products were oxygenated compounds, such as acetol, acrolein, acetaldehyde, acetone, and acetic acid. A noteworthy observation is that acetol is the main liquid product, with its selectivity value rising with temperature up to

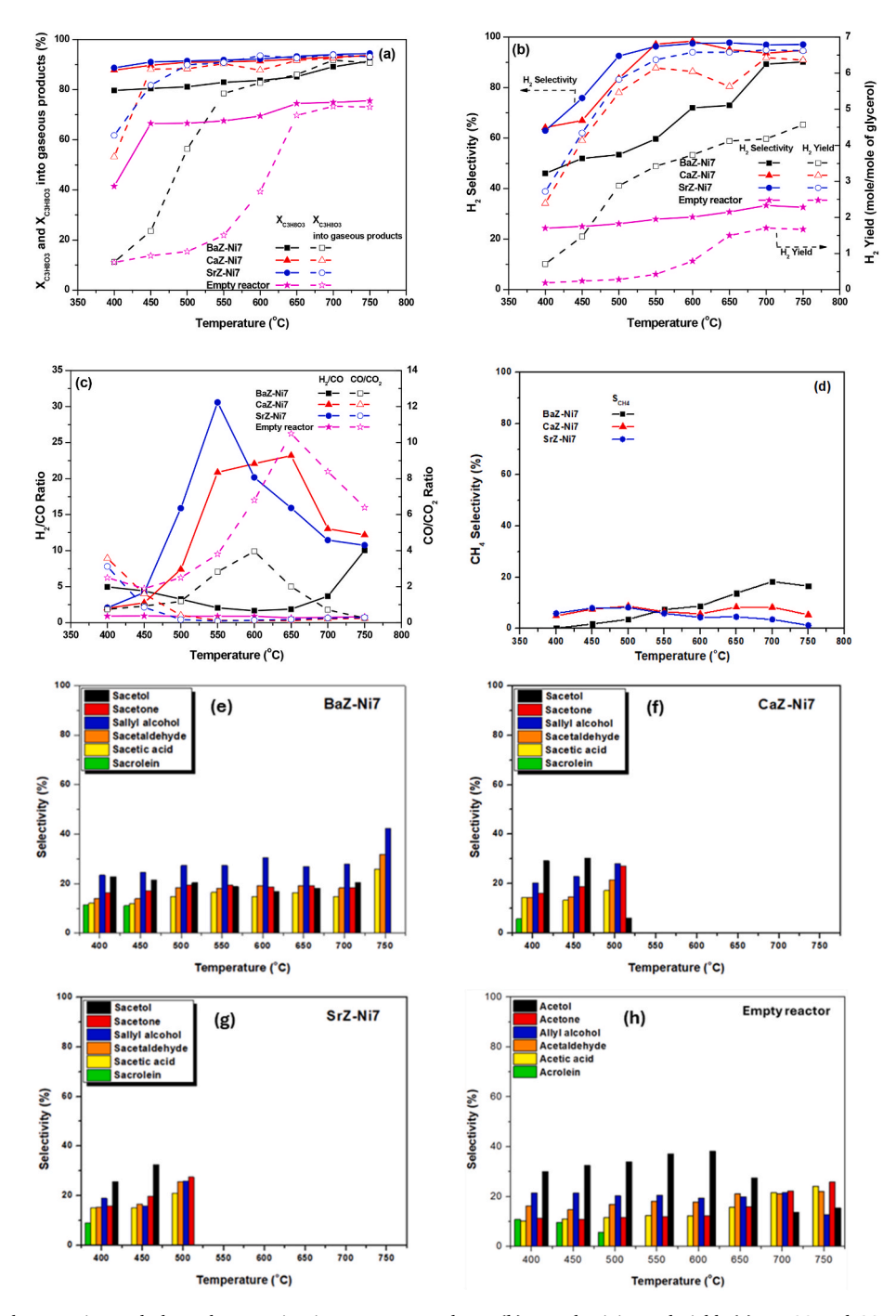


Fig. 7. (a) Total glycerol conversion and glycerol conversion into gaseous products, (b)  $H_2$  selectivity and yield, (c)  $H_2$ /CO and CO/CO<sub>2</sub> molar ratios, (d)  $CH_4$  selectivity, and (e–g) liquid products selectivity for the MeZ-Ni7 catalysts used herein, (e) BaZ-Ni7, (f) CaZ-Ni7, (g) SrZ-Ni7, and (h) Empty reactor. [Results obtained for samples tested under the reaction conditions:  $C_3H_8O_3$  (20 wt %)/ $H_2O$  (total liquid flow rate = 0.12 mL min<sup>-1</sup>)/ $H_2O$  = 38 mL min<sup>-1</sup>, WHSV = 50,000 mL g<sup>-1</sup> h<sup>-1</sup>,  $W_{catalyst}$  = 200 mg, T = 400–750 °C].

600  $^{\circ}\text{C}$  (S<sub>600</sub>  $\approx$  40 %), while the value is decreasing at higher reaction temperatures.

By providing a correlation between the physicochemical characteristics and the catalytic performance for the three different catalysts used herein, it appears that the available specific surface area (SSA) plays a quite important role, since the material with the highest SSA (SrZ-Ni7) displays the best catalytic performance, and the material with the lowest SSA (BaZNi-7) the worst. Another important factor is the Ni reducibility and the Ni-support interaction, as it appears that the less reducible Ni<sup>2+</sup> species initially incorporated into the perovskite lattice ( $\gamma$  peak in H<sub>2</sub>-TPR), which were more plentiful in SrZ-Ni7, are more conducive

towards a higher catalytic activity when compared to Ni originating from segregated NiO in the surface and subsurface ( $\alpha$  and  $\beta$  peaks in H<sub>2</sub>-TPR), which was more plentiful in BaZNi-7. The reduction/exsolution of the aforementioned initially solubilized Ni<sup>2+</sup> species enhances the metal-support interaction, which also affects the surface chemistry. It can be expected, that exsolution alters the electronic properties of the Ni metal, making it more favorable for glycerol adsorption and decomposition (C–C, C–O, and C–H bond scission) [79], whereas the A-site cation segregation that accompanies exsolution can generate hygroscopic surface oxides (e.g., SrO) that can favor water adsorption and dissociation to hydroxyl species [80]. Moreover, taking into account the surface

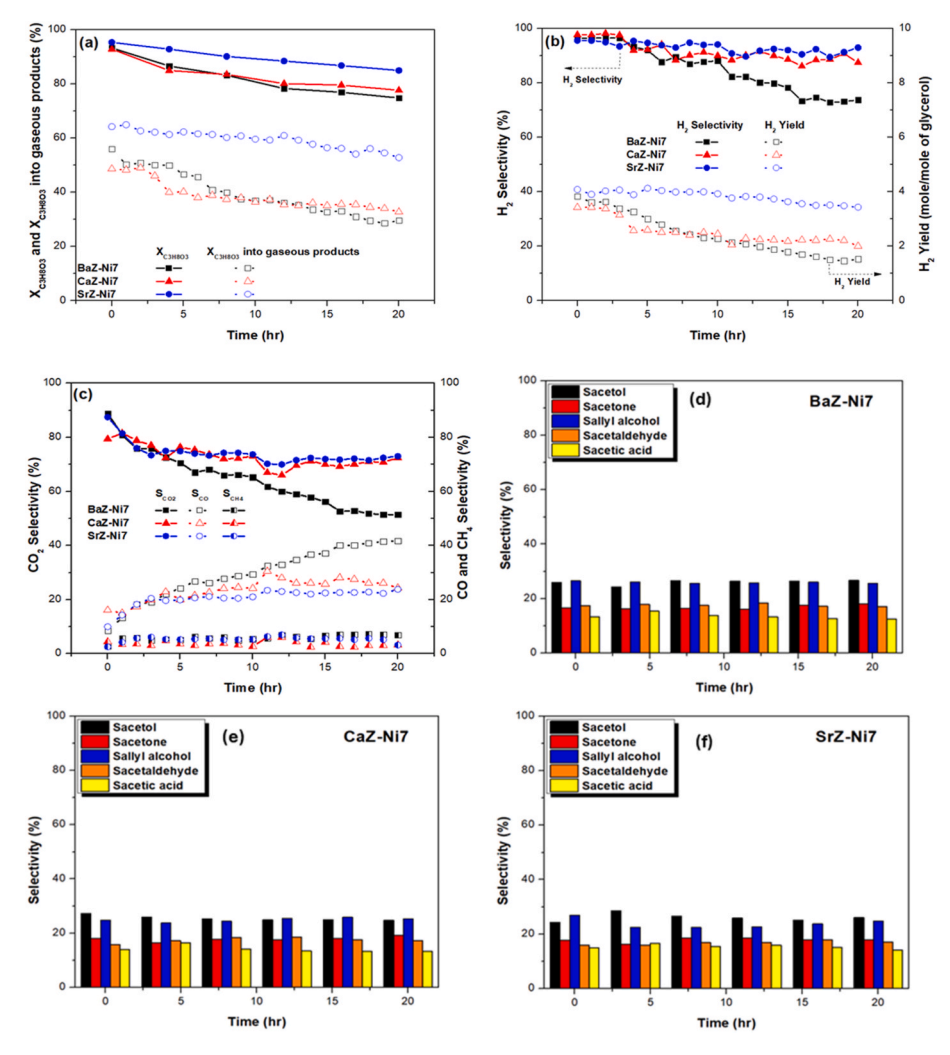


Fig. 8. Time-on-stream experiments for the MeZ-Ni7 catalysts used herein: (a) Total glycerol conversion and glycerol conversion into gaseous products, (b)  $H_2$  selectivity and yield, (c) CO, CO<sub>2</sub> and CH<sub>4</sub> selectivity, and (d-f) liquid products selectivity for (d) BaZ-Ni7, (e) CaZ-Ni7, and (f) SrZ-Ni7. [Results obtained for samples tested under the reaction conditions:  $C_3H_8O_3$  (31 wt %)/ $H_2O$  (total liquid flow rate = 0.12 mL min<sup>-1</sup>)/He = 50 mL min<sup>-1</sup>,  $w_{catalyst}$  = 200 mg, T = 600 °C].

basicity via  $CO_2$ -TPD (Fig. 5), it appears that the weak basic sites play a more important role in the reaction when compared to the highly strong ones.

#### 3.2.3. Time-on-stream stability

The time-on-stream experiments (Fig. 8) were undertaken at harsher reaction conditions, as explained in the experimental part. From the results obtained, SrZ-Ni7 showed an apparently higher catalytic activity and a remarkable catalytic stability. CaZ-Ni7, which was able to roughly match the activity of SrZ-Ni7 under the more favorable reaction conditions of the activity experiments (higher WGFR, Fig. 7), was now shown to be quite inferior to SrZ-Ni7 under these harsher reaction conditions, with a much lower activity for glycerol gasification and H<sub>2</sub> production. BaZ-Ni7 was the least stable of the catalysts, exhibiting a continuous drop in the catalytic activity to the detriment of H<sub>2</sub> production. Carbon-basis CO selectivity also increased over time, leading to a further H<sub>2</sub>/CO ratio drop. In short, SrZ-Ni7 was clearly able to outmatch the other two catalysts regarding the glycerol conversion towards a gaseous products, H<sub>2</sub> productivity, and catalytic stability.

The  $H_2$  yield of SrZ-Ni7 during the stability experiments was *the highest recorded* amongst most of our other works that used the same, harsh, experimental conditions and catalysts with a similar Ni content [12,14,17,20,22–25,27,30] and among the highest reported in the literature [13,15,29,45,47,49,54], as depicted in Table 5.This

exceptional catalytic performance can be attributed to the unique Ni-support interaction in the SrZ-Ni7 catalyst [38]. As shown during the catalyst characterization, the majority of Ni<sup>2+</sup> cations are solubilized into the perovskite lattice following high-temperature calcination. Incorporated into the perovskite lattice, these cations are subsequently driven toward the surface upon high-temperature reduction via the exsolution process [33]. Exsolved nanoparticles typically retain a particularly strong interaction with the perovskite former host and are strongly anchored to their support [33,38,44]. A multitude of published works [33,37,38,42,43,60,81,82] demonstrate the superiority of exsolved systems over impregnated ones when applied in coke-generating catalytic reactions (e.g., dry methane reforming), due to the socketed nature of the exsolved nanoparticles that prevents extensive coking on the metallic Ni surface. Therefore, the higher activity of SrZ-Ni7 over the typical impregnated catalysts (e.g., Ni/Al<sub>2</sub>O<sub>3</sub> and Ni/ZrO<sub>2</sub>) can be ascribed to the presence of these well-dispersed and socketed exsolved Ni nanoparticles with a strong metal-support interaction. Overall, a strong metal-support interaction can restrict coke formation and metal nanoparticle sintering, enhance the electron transfer and the adsorption of reactants, as well as inhibit certain side-reactions, like CO<sub>x</sub> methanation, thereby improving the catalytic activity and stability [56,83,84].

**Table 5** Summary of experimental studies on the GSR reaction using different catalysts ( $X_G = \text{glycerol conversion}$ ,  $Y_{H2} = H_2$  yield).

T (°C)	Feedstock moral ratio	Catalyst	WHSV	$X_G$	$Y_{H2}$	Ref.
600	$S/C_3H_8O_3$ = 9/1	Ni/SrZrO <sub>3</sub> (SrZ- Ni7, Ni = 9.3 wt%)	50,000 mL g <sup>-1</sup> h <sup>-1</sup>	85 %	3.5 mol/ mol of C <sub>3</sub> H <sub>8</sub> O <sub>3</sub>	This work
650	$S/C_3H_8O_3$ $= 9/1$	Ni/Ce-Sm-10Cu (Ni = 8 wt%)	50,000 mL g <sup>-1</sup> h <sup>-1</sup>	90 %	3.7 mol/ mol of C <sub>3</sub> H <sub>8</sub> O <sub>3</sub>	[12]
600	$S/C_3H_8O_3$ $= 9/1$	Ni/AlCeO <sub>3</sub> (Ni = 8 wt%)	50,000 mL g <sup>-1</sup> h <sup>-1</sup>	75 %	2.2 mol/ mol of C <sub>3</sub> H <sub>8</sub> O <sub>3</sub>	[14]
600	$S/C_3H_8O_3$ $= 9/1$	$Ni/Y_2O_3$ - $ZrO_2$ (Ni = 8 wt%)	50,000 mL g <sup>-1</sup> h <sup>-1</sup>	67 %	2.2 mol/ mol of C <sub>3</sub> H <sub>8</sub> O <sub>3</sub>	[20]
600	$S/C_3H_8O_3$ $= 9/1$	$\begin{array}{l} Rh/10MgOAl_2O_3 \\ (Rh=0.5 \text{ wt\%}) \end{array}$	50,000 mL g <sup>-1</sup> h <sup>-1</sup>	90 %	3.0 mol/ mol of C <sub>3</sub> H <sub>8</sub> O <sub>3</sub>	[22]
600	$S/C_3H_8O_3$ $= 9/1$	$Ni/$ $CaO-MgO-Al_2O_3$ $(Ni = 8 \text{ wt\%})$	50,000 mL g <sup>-1</sup> h <sup>-1</sup>	80 %	2.2 mol/ mol of C <sub>3</sub> H <sub>8</sub> O <sub>3</sub>	[25]
600	$S/C_3H_8O_3$ $= 9/1$	0.5Pt/CeO <sub>2</sub> -Al <sub>2</sub> O <sub>3</sub> (Pt = 0.5 wt%)	50,000 mL g <sup>-1</sup> h <sup>-1</sup>	80 %	1.0 mol/ mol of C <sub>3</sub> H <sub>8</sub> O <sub>3</sub>	[27]
600	$S/C_3H_8O_3$ $= 9/1$	Ni/Attapulgite (Ni = 8 wt%)	50,000 mL g <sup>-1</sup> h <sup>-1</sup>	65 %	1.0 mol/ mol of C <sub>3</sub> H <sub>8</sub> O <sub>3</sub>	[30]
550	S/C = 3	Ni/La <sub>2</sub> O <sub>3</sub> (Ni = 23.4 wt%)	2.5 h <sup>-1</sup> (GHSV)	100 %	2.5 mol/ mol of C <sub>3</sub> H <sub>8</sub> O <sub>3</sub>	[45]

#### 3.3. Spent catalyst characterization

The nature of the deposited carbon on the spent catalysts (i.e., after the 20h time-on-stream experiments) was examined using Raman, TEM, and TPO. From the results obtained using Raman analysis (Fig. 9), two characteristic peaks at around 1345 and 1580 cm<sup>-1</sup> were observed, which can be attributed to coke deposits. These peaks are respectively assigned to the D-band (1344 cm<sup>-1</sup>), associated with the vibrations of carbon atoms with dangling bonds in an amorphous carbon structure, and the G-band (1580 cm<sup>-1</sup>), that corresponds to graphitic carbon with a high degree of crystallinity [85]. The intensity ratio of the D-band to the G-band  $(I_D/I_G)$  serves as a measure of the graphitization level. In particular, lower values of I<sub>D</sub>/I<sub>G</sub> suggest increased crystallinity, reflecting a greater presence of graphitized carbon, which in turn contributes to the deactivation of the supported catalytically active sites [20]. The I<sub>D</sub>/I<sub>G</sub> ratio of the CaZ-Ni7 and BaZNi-7 spent samples was calculated at 1.5 and 1.1, respectively, meaning that the coke deposits on BaZNi-7 had increased crystallinity and graphitization level, thus corroborating the lower catalytic stability of this catalyst (Fig. 8). Since the Raman peaks of SrZ Ni7 had a very low intensity, the calculation of the I<sub>D</sub>/I<sub>G</sub> ratio for this sample would not be reliable. Furthermore, it is important to note that the SrZ-Ni7 sample showed no clear Raman peaks despite the measurement being repeated for approximately 20 different regions (the plotted one has the maximum intensity that could be detected). This indicates much more reduced coking for this catalyst, corroborating its higher catalytic activity and stability (Fig. 8).

Furthermore, TPO characterization was conducted on the spent catalysts (Fig. 10). From Fig. 10, we can observe very high noise/fluctuations in the TCD signal, which are indicative of the quite low amount of coke deposition in all catalytic materials. This is expected in our current work since, as already discussed, the strong metal support interaction (SMSI) originating from Ni<sup>2+</sup> exsolution to the surface disfavors coke accumulation. However, when comparing the different catalysts, SrZNi-7 displays the least amount of coke combusted, corroborating the catalytic stability results (Fig. 8), as well as the Raman results (Fig. 9) of the spent catalysts. For the other spent catalysts, CaZNi-7 displays some amount of coke combusted at lower

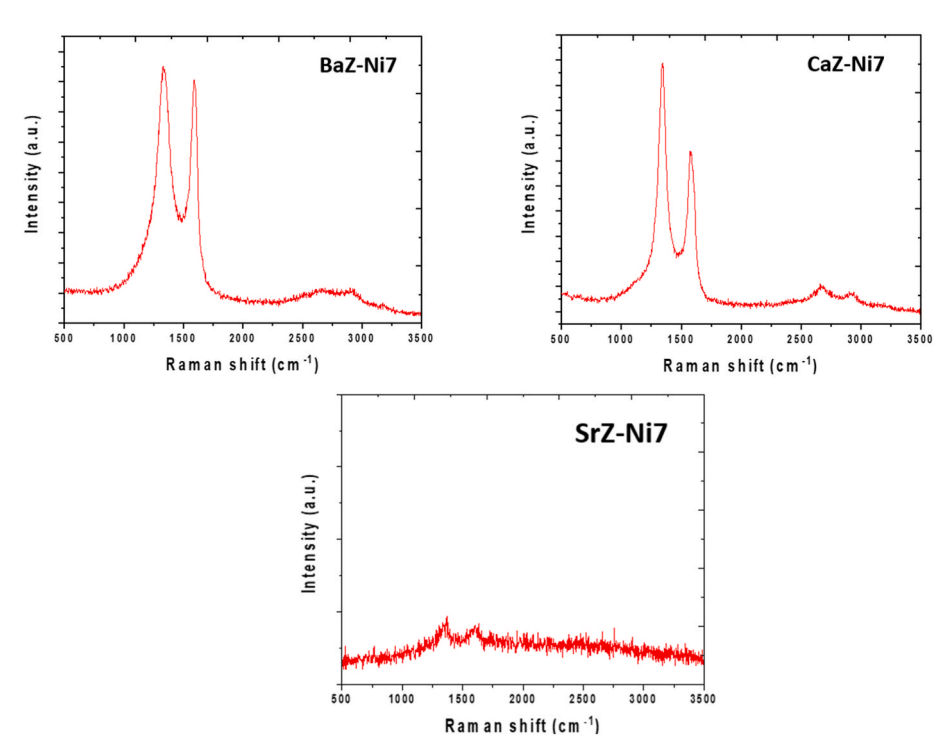
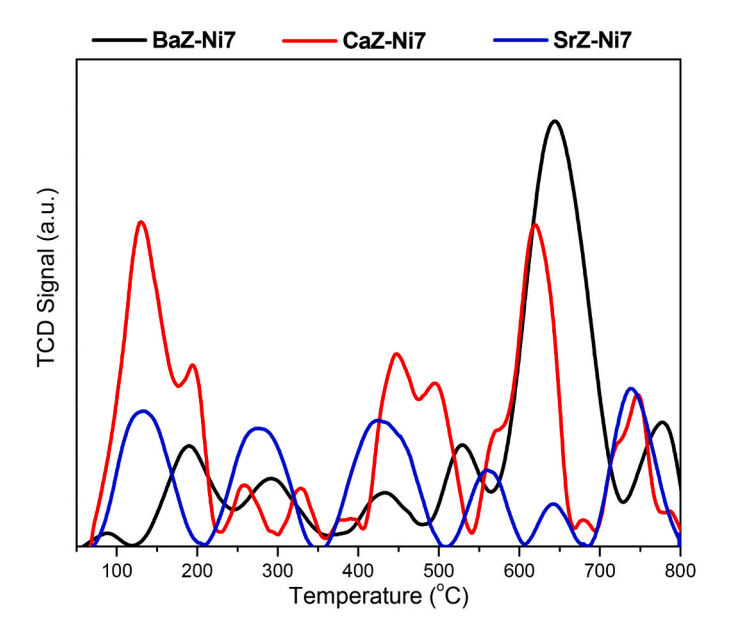


Fig. 9. Raman spectra of the MeZ-Ni7 spent catalysts. [Results obtained for samples tested under experimental protocol #2].



**Fig. 10.** TPO profiles of the MeZ-Ni7 spent catalysts. [Results obtained for samples tested under experimental protocol #2].

temperatures, due to amorphous/disordered coke deposits, and some amount of coke combusted at higher temperatures, due to crystalline/graphitic carbon [80]. On the other hand, BaZNi-7 exhibits the highest intensity peak at higher temperatures, indicating a more crystalline/graphitic nature of deposited coke in this catalyst, in agreement with the Raman results (Fig. 9), which is hard to be oxidized/gasified during the catalytic reaction.

In line with the Raman and TPO results, the HAADF-STEM images obtained for the spent catalysts (Fig. 11) reveal limited carbon accumulation for all samples. However, when comparing them, the BaZ-Ni7 catalyst exhibits the highest amount, while SrZ-Ni7 the least. The high resistance to carbon deposition in all samples, and in particular over SrZ-Ni7, can be attributed to the strong Ni-support interaction, since the images reveal that the Ni nanoparticles are socketed into the perovskite structure, retaining their morphology and high dispersion under exposure to harsh reaction conditions [38,56]. Such anti-coking properties are commonly attributed to the exsolution process, which yields well-dispersed nanoparticles with very strong metal-support interaction. This results in catalytic materials that are less prone toward extensive carbon growth over the exposed metallic Ni surface, as well as nanoparticle sintering [33,38,42,44,56].

### 4. Conclusions

In the study reported herein, Ni catalysts supported on CaZrO<sub>3</sub>, SrZrO<sub>3</sub>, and BaZrO<sub>3</sub> perovskite oxides were synthesized via the auto-

combustion method and subsequently examined in terms of catalytic activity and time-on-stream stability during the glycerol steam reforming reaction (GSR). Before the reaction, the surface and bulk properties of the materials were examined using XRD,  $N_2$  physisorption,  $H_2$ -TPR,  $H_2$  pulse chemisorption, and  $CO_2$ -TPD. Post-reaction, the catalysts were examined using Raman, TPO, and TEM/HAADF-STEM to determine the causes of catalyst deactivation.

Catalytic activity experiments showed that CaZ-Ni7 and SrZ-Ni7 effectively eliminate all liquid products (acetol, acetone, allyl alcohol, acetaldehyde, and acetic acid) at reaction temperatures higher than 500  $^{\circ}\text{C}$ , converting the entirety of glycerol into gaseous products, with SrZNi-7 exhibiting the highest H $_2$  yield (>6 mol H $_2$ /mol of glycerol for temperatures higher than 500  $^{\circ}\text{C}$ ). This exceptional performance is attributed to the higher Ni dispersion, increased availability of active sites to dissociate  $C_3H_8O$  and  $H_2O$  molecules, and a more favorable and stronger Ni-support interaction. It is noted that the activity for SrZ-Ni7 is among the highest reported in the literature.

Catalytic stability experiments undertaken at harsher reaction conditions showed that the SrZ-Ni7 catalyst had a very stable performance, which was superior to the BaZ-Ni7 and CaZ-Ni7 catalysts. This behavior is attributed to its unique Ni-support interaction, where some  $\mathrm{Ni}^{2+}$  cations are initially solubilized into the perovskite lattice following high-temperature calcination. These cations then migrate to the surface during high-temperature reduction via the exsolution process forming nanoparticles, which, during the reaction, are less prone to deactivation via coking and sintering.

#### CRediT authorship contribution statement

Igor Luisetto: Writing – original draft, Resources, Investigation, Formal analysis, Data curation, Conceptualization. Nikolaos D. Charisiou: Writing – review & editing, Writing – original draft, Validation, Methodology, Investigation, Formal analysis, Data curation, Conceptualization. Anastasios I. Tsiotsias: Writing – original draft, Formal analysis. Angeliki I. Latsiou: Writing – original draft, Formal analysis. Georgios Siakavelas: Writing – original draft, Formal analysis. Victor Sebastian: Writing – review & editing, Formal analysis, Data curation. Runduo Zhang: Writing – review & editing. Elisabetta Di Bartolomeo: Writing – review & editing, Validation, Resources, Formal analysis, Data curation. Maria A. Goula: Writing – review & editing, Visualization, Supervision, Resources, Project administration, Methodology, Conceptualization.

# **Declaration of competing interest**

The authors declare that they have no known competing financial interests or personal relationships that could have appeared to influence the work reported in this paper.

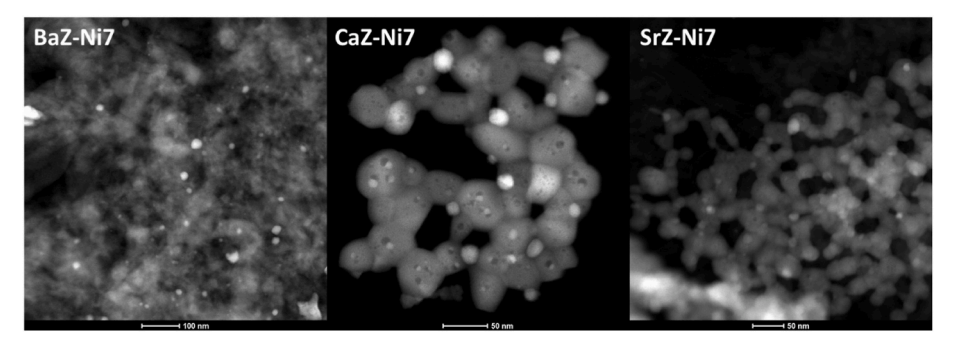


Fig. 11. HAADF-STEM images of the MeZ-Ni7 spent catalysts. [Results obtained for samples tested under experimental protocol #2].

#### Appendix A. Supplementary data

Supplementary data to this article can be found online at https://doi.org/10.1016/j.jjhydene.2025.04.246.

#### References

- [1] Saravanan A, Senthil Kumar P, Vo DVN, Jeevanantham S, Bhuvaneswari V, Anantha Narayanan V, Yaashikaa PR, Swetha S, Reshma B. A comprehensive review on different approaches for CO<sub>2</sub> utilization and conversion pathways. Chem Eng Sci 2021;236:116515.
- [2] Siakavelas GI, Charisiou ND, AlKhoori A, AlKhoori S, Sebastian V, Hinder SJ, Baker MA, Yentekakis IV, Polychronopoulou K, Goula MA. Highly selective and stable Ni/La-M (M=Sm, Pr, and Mg)-CeO<sub>2</sub> catalysts for CO<sub>2</sub> methanation. J CO2 Util 2021:51:101618.
- [3] Latsiou AI, Charisiou ND, Frontistis Z, Bansode A, Goula MA. CO<sub>2</sub> hydrogenation for the production of higher alcohols: recent trends, challenges and opportunities. Catal Today 2023;420:114179.
- [4] Douvartzides S, Charisiou ND, Wang W, Papadakis VG, Polychronopoulou K, Goula MA. Catalytic fast pyrolysis of agricultural residues and dedicated energy crops for the production of high energy density transportation biofuels. Part II: catalytic Research. Renew. Energ. 2022;189:315–38.
- [5] Arias A, Nika CE, Vasilaki V, Feijoo G, Moreira MT, Katsou E. Assessing the future prospects of emerging technologies for shipping and aviation biofuels: a critical review. Renew Sustain Energy Rev 2024;197:114427.
- [6] Tsiotsias A, Hafeez S, Charisiou ND, Al-Salem SM, Manos G, Constantinou A, AlKhoori S, Sebastian V, Hinder SJ, Baker MA, Polychronopoulou K, Goula MA. Selective catalytic deoxygenation of palm oil to produce green diesel over Ni Catalysts Supported on ZrO<sub>2</sub> and CeO<sub>2</sub>-ZrO<sub>2</sub>: experimental and process simulation modelling studies. Renew. Energ. 2023;206:582–96.
- [7] Pandey S. Narayanan I, Selvaraj R, Varadavenkatesan T, Vinayagam R. Biodiesel production from microalgae: a comprehensive review on influential factors, transesterification processes, and challenges. Fuel 2024;367:131547.
- [8] Dabbawala AA, Al Maksoud W, Abou-Hamad E, Charisiou ND, Latsiou AI, AlKhoori S, Hinder SJ, Baker MA, Kobayashi Y, Goula MA, Polychronopoulou K. Tuning of the acid sites in the zeolite-alumina composite Ni catalysts and their impact on the palm oil hydrodeoxygenation reaction. Chem. Eng. J. 2024;493: 152351.
- [9] Soodesh CY, Seriyala AK, Navjot P, Chattopadhyay P, Rozhkova N, Michalkiewicz B, Chatterjee S, Roy B. Carbonaceous catalysts (biochar and activated carbon) from agricultural residues and their application in production of biodiesel: a review. Chem Eng Res Des 2024;203:759–88.
- [10] Manosak R, Limpattayanate S, Hunsom M. Sequential-refining of crude glycerol derived from waste used-oil methyl ester plant via a combined process of chemical and adsorption. Fuel Process Technol 2011;92:92–9.
- [11] Charisiou ND, Polychronopoulou K, Asif A, Goula MA. The potential of glycerol and phenol towards H<sub>2</sub> production using steam reforming reaction: a review. Surf Cost Technol 2018:352-92-111
- [12] Polychronopoulou K, Charisiou N, Papageridis K, Sebastian V, Hinder S, Dabbawala A, Alkhoori A, Baker M, Goula M. The effect of Ni addition onto a Cubased ternary support on the H<sub>2</sub> production over glycerol steam reforming reaction. Nanomaterials 2018;8:931.
- [13] Qureshi F, Yusuf M, Pasha AA, Khan HW, Imteyaz B, Irshad K. Sustainable and energy efficient hydrogen production via glycerol reforming techniques: a review. Int J Hydrogen Energy 2022;47:41397–420.
- [14] Charisiou ND, Siakavelas G, Dou B, Sebastian V, Baker MA, Hinder SJ, Polychronopoulou K, Goula MA. Nickel supported on AlCeO<sub>3</sub> as a highly selective and stable catalyst for hydrogen production via the glycerol steam reforming reaction. Catalysts 2019;9:411.
- [15] Bac S, Keskin S, Avci AK. Recent advances in materials for high purity H<sub>2</sub> production by ethanol and glycerol steam reforming. Int J Hydrogen Energy 2020; 45:34888–917.
- [16] Polychronopoulou K, Dabbawala AA, Sajjad M, Singh N, Anjum DH, Baker MA, Charisiou ND, Goula MA. Hydrogen production via steam reforming of glycerol over Ce-La-Cu-O ternary oxide catalyst: an experimental and DFT study. Appl Surf Sci 2022:586:152798.
- [17] Charisiou ND, Siakavelas G, Papageridis KN, Sebastian V, Hinder SJ, Baker MA, Polychronopoulou K, Goula MA. The influence of SiO<sub>2</sub> doping on the Ni/ZrO<sub>2</sub> supported catalyst for hydrogen production through the glycerol steam reforming reaction. Catal Today 2019;319:206–19.
- [18] Chen H, Ding Y, Cong NT, Dou B, Dupont V, Ghadiri M, Williams PT. A comparative study on hydrogen production from steam-glycerol reforming: thermodynamics and experimental. Renew. Energ. 2011;36:779–88.
- [19] Adhikari S, Fernando S, Gwaltney SR, Filip To SD, Bricka RM, Steele PH, Haryanto A. A thermodynamic analysis of hydrogen production by steam reforming of glycerol. Int J Hydrogen Energy 2007;32:2875–80.
- [20] Charisiou ND, Siakavelas G, Tzounis L, Dou B, Sebastian V, Hinder SJ, Baker MA, Polychronopoulou K, Goula MA. Ni/Y<sub>2</sub>O<sub>3</sub>–ZrO<sub>2</sub> catalyst for hydrogen production through the glycerol steam reforming reaction. Int J Hydrogen Energy 2020;45: 10442–60.
- [21] Goula MA, Charisiou ND, Papageridis KN, Siakavelas G. Influence of the synthesis method parameters used to prepare nickel-based catalysts on the catalytic performance for the glycerol steam reforming reaction. Chin J Catal 2016;37: 1949–65.

- [22] Charisiou ND, Italiano C, Pino L, Sebastian V, Vita A, Goula MA. Hydrogen production via steam reforming of glycerol over Rh/γ-Al<sub>2</sub>O<sub>3</sub> catalysts modified with CeO<sub>2</sub>, MgO or La<sub>2</sub>O<sub>3</sub>. Renew. Energ. 2020;162:908–25.
- [23] Papageridis KN, Charisiou ND, Siakavelas G, Avraam DG, Tzounis L, Kousi K, Goula MA. Comparative study of Ni, Co, Cu supported on γ-alumina catalysts for hydrogen production via the glycerol steam reforming reaction. Fuel Process Technol 2016;152:156–75.
- [24] Charisiou ND, Siakavelas G, Palpigrades KN, Baklavaridis A, Tzounis L, Polychronopoulou K, Goula MA. Hydrogen production via the glycerol steam reforming reaction over nickel supported on alumina and lanthana-alumina catalysts. Int J Hydrogen Energy 2017;42:13039–60.
- [25] Charisiou ND, Papageridis KN, Tzounis L, Sebastian V, Baker MA, Hinder SJ, AlKetbi M, Polychronopoulou K, Goula MA. Ni supported on CaO-MgO-Al<sub>2</sub>O<sub>3</sub> as a highly selective and stable catalyst for H<sub>2</sub> production via the glycerol steam reforming reaction. Int J Hydrogen Energy 2019;44:256–73.
- [26] Senseni AZ, Rezaei M, Meshkani F. Glycerol steam reforming over noble metal nanocatalysts. Chem Eng Res Des 2017;123:360-6.
- [27] Charisiou ND, Siakavelas GI, Papageridis KN, Motta D, Dimitratos N, Sebastian V, Polychronopoulou K, Goula MA. The effect of noble metal (M: Ir, Pt, Pd) on M/ Ce<sub>2</sub>O<sub>3</sub>·γ-Al<sub>2</sub>O<sub>3</sub> catalysts for hydrogen production via the steam reforming of glycerol. Catalysts 2020;10:790.
- [28] Charisiou ND, Papageridis KN, Siakavelas G, Tzounis L, Kousi K, Baker MA, Hinder SJ, Sebastian V, Polychronopoulou K, Goula MA. Glycerol steam reforming for hydrogen production over nickel supported on alumina, zirconia and silica catalysts. Top Catal 2017;60:1226–50.
- [29] Macedo MS, Kraleva E, Ehrich H, Soria MA, Madeira LM. Ni-based catalysts supported on La/AlZn/AlLa oxides for hydrogen production via glycerol steam reforming. Renew. Energ. 2024;223:120076.
- [30] Charisiou ND, Sebastian V, Hinder SJ, Baker MA, Polychronopoulou K, Goula MA. Ni catalysts based on attapulgite for hydrogen production through the glycerol steam reforming reaction. Catalysts 2019;9:650.
- [31] Wang Y, Chen Y, Zhu S, Song D, Ai T, He S, Luo Y. Ni/CeO2 catalysts for glycerol steam reforming: effect of calcination modes on the catalytic performance. Int J Hydrogen Energy 2024;65:804–16.
- [32] Royer S, Duprez D, Can F, Courtois X, Batiot-Dupeyrat C, Laassiri S, Alamdari H. Perovskites as substitutes of noble metals for heterogeneous catalysis: dream or reality. Chem. Rev. 2014;114:10292–368.
- [33] Kousi K, Tang C, Metcalfe IS, Neagu D. Emergence and future of exsolved materials. Small 2021;17:2006479.
- [34] Latsiou A, Lykos C, Bairamis F, Konstantinou I. Synthesis and characterization of LaCo<sub>x</sub>Ni<sub>1-x</sub>O<sub>3</sub> perovskites as heterogeneous catalysts for phenolics degradation by persulfate activation. J Chem Technol Biotechnol 2022;97:3467–80.
- [35] Polychronopoulou K, Charisiou ND, Siakavelas G, AlKhoori AA, Sebastian V, Hinder SJ, Baker MA, Goula MA. Ce-Sm-xCu cost efficient catalysts for H<sub>2</sub> production through the glycerol steam reforming reaction. Sustain Energy Fuels 2019;3:673–91.
- [36] Goula MA, Charisiou ND, Pandis PK, Stathopoulos VN. Ni/apatite-type lanthanum silicate supported catalyst for the glycerol steam reforming reaction. RCS Advances 2016;6:78954–8.
- [37] Rudolph B, Tsiotsias A, Ehrhardt B, Gross S, Dolcet P, Haas S, Charisiou ND, Goula MA, Mascotto S. Nanoparticle exsolution from nanoporous perovskites for highly active and stable biogas dry reforming catalysts. Advanced Sci 2023;10: 2205890
- [38] Neagu D, Oh TS, Miller DN, Ménard H, Bukhari SM, Gamble SR, Gorte RJ, Vohs JM, Irvine JTS. Nano-socketed nickel particles with enhanced coking resistance grown in situ by redox exsolution. Nat Commun 2015;6:8120.
- [39] Hayakawa T, Suzuki S, Nakamura J, Uchijima T, Hamakawa S, Suzuki K, Shishido T, Takehira K. CO<sub>2</sub> reforming of CH<sub>4</sub> over Ni/perovskite catalysts prepared by solid phase crystallization method. Appl. Catal. A-Gen. 1999;183: 273–85.
- [40] Sekine Y, Mukai D, Murai Y, Tochiya S, Izutsu Y, Sekiguchi K, Hosomura N, Arai H, Kikuchi E, Sugiura Y. Steam reforming of toluene over perovskite-supported Ni catalysts. Appl. Catal. A-Gen. 2013;451:160–7.
- [41] Zhang Z, Ou Z, Qin C, Ran J, Wu C. Roles of alkali/alkaline earth metals in steam reforming of biomass tar for hydrogen production over perovskite supported Ni catalysts. Fuel 2019;257:116032.
- [42] Wei T, Jia L, Zheng H, Chi B, Pu J, Li J. LaMnO<sub>3</sub>-based perovskite with in-situ exsolved Ni nanoparticles: a highly active, performance stable and coking resistant catalyst for CO<sub>2</sub> dry reforming of CH<sub>4</sub>. Appl. Catal. A-Gen. 2018;564:199–207.
- [43] Tsiotsias A, Ehrhardt B, Rudolph B, Nodari L, Kim S, Jung W, Charisiou ND, Goula MA, Mascotto S. Modulating bimetallic Fe-Ni exsolution to tune the CO<sub>2</sub>assisted ethane dehydrogenation and reforming pathways. ACS Nano 2022;16: 8904–16.
- [44] Neagu D, Kyriakou V, Roiban IL, Aouine M, Tang C, Caravaca A, Kousi K, Schreur-Piet I, Metcalfe IS, Vernoux P, Van De Sanden MCM, Tsampas MN. In situ observation of nanoparticle exsolution from perovskite oxides: from atomic scale mechanistic insight to nanostructure tailoring. ACS Nano 2019;13:12996–3005.
- [45] Wu G, Li S, Zhang C, Wang T, Gong J. Glycerol steam reforming over perovskitederived nickel-based catalysts. Appl Catal B Environ 2014;144:277–85.
- [46] Aman D, Radwan D, Ebaid M, Mikhail S, van Steen E. Comparing nickel and cobalt perovskites for steam reforming of glycerol. Mol Catal 2018;452:60–7.
- [47] Franchini CA, Aranzaez W, Duarte de Farias AM, Pecchi G, Fraga MA. Cesubstituted LaNiO<sub>3</sub> mixed oxides as catalyst precursors for glycerol steam reforming. Appl Catal B Environ 2014;147:193–202.

- [48] Ramesh S, Yang EH, Jung JS, Moon DJ. Copper decorated perovskite an efficient catalyst for low temperature hydrogen production by steam reforming of glycerol. Int J Hydrogen Energy 2015;40:11428–35.
- [49] Ramesh S, Venkatesha NJ. Template free synthesis of Ni-perovskite: an efficient catalyst for hydrogen production by steam reforming of bioglycerol. ACS Sustainable Chem Eng 2017;5:1339–46.
- [50] Kamonsuangkasem K, Therdthianwong S, Therdthianwong A, Thammajak N. Remarkable activity and stability of Ni catalyst supported on CeO<sub>2</sub>-Al<sub>2</sub>O<sub>3</sub> via CeAlO<sub>3</sub> perovskite towards glycerol steam reforming for hydrogen production. Appl Catal B Environ 2017;218:650–63.
- [51] Dieuzeide ML, Laborde M, Amadeo N, Cannilla C, Bonura G, Frusteri F. Hydrogen production by glycerol steam reforming: how Mg doping affects the catalytic behaviour of Ni/Al<sub>2</sub>O<sub>3</sub> catalysts. Int J Hydrogen Energy 2016;41:157–66.
- [52] Feng P, Huang K, Xu Q, Qi W, Xin S, Wei T, Liao L, Yan Y. Ni supported on the CaO modified attapulgite as catalysts for hydrogen production from glycerol steam reforming. Int J Hydrogen Energy 2020;45:8223–33.
- [53] Calles JA, Carrero A, Vizcaíno AJ, García-Moreno L. Hydrogen production by glycerol steam reforming over SBA-15-supported nickel catalysts: effect of alkaline earth promoters on activity and stability. Catal Today 2014;227:198–206.
- [54] Kim SH, Jung JS, Yang EH, Lee KY, Moon DJ. Hydrogen production by steam reforming of biomass-derived glycerol over Ni-based catalysts. Catal Today 2014; 228:145-51
- [55] Ruocco C, De Caprariis B, Palma V, Petrullo A, Ricca A, Scarsella M, De Filippis P. Methane dry reforming on Ru perovskites, AZrRuO<sub>3</sub>: influence of preparation method and substitution of A cation with alkaline earth metals. J CO2 Util 2019; 30:222-31
- [56] Dama S, Ghodke SR, Bobade R, Gurav HR, Chilukuri S. Active and durable alkaline earth metal substituted perovskite catalysts for dry reforming of methane. Appl Catal B Environ 2018;224:146–58.
- [57] Varma A, Mukasyan AS, Rogachev AS, Manukyan KV. Solution combustion synthesis of nanoscale materials. Chem. Rev. 2016;16:14493–586.
- [58] Banasri R, Fuierer PA. Synthesis of cobalt-doped bismuth vanadate by combustionsynthesis: influence of fuel on phase content and morphology. J Mater Res 2009; 24:3078–86
- [59] Luisetto I, Mancini MR, Della Seta L, Chierchia R, Vanga G, Grilli ML, Stendardo S. CaO-CaZrO<sub>3</sub> mixed oxides prepared by auto-combustion for high temperature CO<sub>2</sub> capture: the Effect of CaO content on cycle stability. Metals 2020;10:750.
- [60] Prioriello A, Duranti L, Luisetto I, Sanna F, Larosa C, Grilli ML, Bartolomeo ED. Structured catalyst for indirect internal reforming (IIR) of biogas in solid oxide fuel cell (SOFC). Catalysts 2023;13:1129.
- [61] Goodenough JB. Electronic and ionic transport properties and other physical aspects of perovskites. Rep Prog Phys 2004;67:1915.
- [62] Katsumata T, Suzuki R, Satoh N, Suzuki S, Nokashima M, Inaguma Y, Mori D, Aimi A, Yoneda Y. Synthesis of new perovskite-type oxyfluorides, BalnO<sub>2</sub>F and comparison of the structure among perovskite-type oxyfluorides. J Solid State Chem 2019:279:120919.
- [63] Teli NA, Want B. Electronic, magnetic, elastic and optical properties of Ba<sub>2</sub>CoTaO<sub>6</sub> double perovskite oxide: a DFT study. J. Magn Magn Matter. 2024;601:172183.
- [64] Holzwarth U, Gibson N. The Scherrer equation versus the 'Debye-Scherrer equation'. Nat Nanotechnol 2011;6:534. 534.
- [65] Williamson GK, Hall WH. X-ray line broadening from filed aluminium and wolfram. Acta Metall Mater 1953;1:22–31.
- [66] Khorsand Zak A, Abd Majid WH, Abrishami ME, Yousefi R. X-ray analysis of ZnO nanoparticles by Williamson-Hall and size-strain plot methods. Solid State Sci 2011;13:251-6
- [67] Thommes M, Kaneko K, Neimark AV, Olivier JP, Rodriguez-Reinoso F, Rouquerol J, Sing KSW. Physisorption of gases, with special reference to the

- evaluation of surface area and pore size distribution (IUPAC Technical Report). Pure Appl Chem 2015;87:1051.
- [68] Lux S, Baldauf-Sommerbauer G, Siebenhofer M. Hydrogenation of inorganic metal carbonates: a review on its potential for carbon dioxide utilization and emission reduction. ChemSusChem 2018;11:3357–75.
- [69] Dow W-P, Wang Y-P, Huang T-J. Yttria-stabilized zirconia supported copper oxide catalyst: I. Effect of oxygen vacancy of support on copper oxide reduction. J Catal 1996;160:155–70.
- [70] Shirpour M, Merkle R, Maier J. Evidence for space charge effects in Y-doped BaZrO<sub>3</sub> from reduction experiments. Solid State Ionics 2012;216:1–5.
- [71] Wang Z, Liu B, Lin J. Highly effective perovskite-type BaZrO<sub>3</sub> supported Ru catalyst for ammonia synthesis. Appl. Catal. A-Gen. 2013;458:130–6.
- [72] Georgiadis AG, Tsiotsias AI, Siakavelas G, Charisiou ND, Ehrhardt B, Sebastian V, Hinder SJ, Baker MA, Mascotto S, Goula MA. An experimental and theoretical approach for the biogas dry reforming reaction using perovskite-derived La<sub>0.8</sub>RE<sub>0.2</sub>NiO<sub>3.6</sub> catalysts (RE = Sm, Pr, Ce). Renew. Energ. 2024;227:120511.
- [73] de Caprariis B, de Filippis P, Palma V, Petrullo A, Ricca A, Ruocco C, Rh Scarsella M. Ru and Pt ternary perovskites type oxides BaZr<sub>(1-x)</sub>Me<sub>x</sub>O<sub>3</sub> for methane dry reforming. Appl. Catal. A-Gen. 2016;517:47–55.
- [74] Aramendía MA, Borau V, Jiménez C, Marinas JM, Moreno A. Comparative measurements of the dispersion of Pd catalyst on SiO<sub>2</sub> AlPO<sub>4</sub> support using TEM and H<sub>2</sub> chemisorption. Colloids Surf 1996;106:161–5.
- [75] Steiger P, Delmelle R, Foppiano D, Holzer L, Heel A, Bachtegaal M, Krocher O, Ferri D. Structural reversibility and nickel particle stability in lanthanum iron nickel perovskite-type catalysts. ChemSusChem 2017;10:2505–17.
- [76] Wang Y, Zhu S, Lu J, He S, Lu H, Song D, Chen D, Luo Y. Novel nanowire self-assembled hierarchical GeO<sub>2</sub> microspheres loaded with nickel-based catalysts for hydrogen production from steam reforming of glycerol. Fuel Process Technol 2023; 243. Article 107677.
- [77] Tsiotsias AI, Charisiou ND, Yentekakis IV, Goula MA. The role of alkali and alkaline earth metals in the CO<sub>2</sub> methanation reaction and the combined capture and methanation of CO<sub>2</sub>. Catalysts 2020;10:812.
- [78] Mehrpooya M, Ghorbani B, Abedi H. Biodiesel production integrated with glycerol steam reforming process, solid oxide fuel cell (SOFC) power plant. Energy Convers Manag 2020;206:112467.
- [79] Ramos-Castillo CM, Torres-Pacheco L, Álvarez-Contreras L, Argona N, Guerra-Balcázar M. Tuning the d-band center of nickel bimetallic compounds for glycerol chemisorption: a density functional study, vol. 30; 2025. p. 744.
- [80] Tsiotsias AI, Charisiou ND, AlKhoori A, Gaber S, Sebastian V, Hinder SJ, Baker MA, Polychronopoulou K, Goula MA. Towards maximizing conversion of ethane and carbon dioxide into synthesis gas using highly stable Ni-perovskite catalysts. J CO<sub>2</sub> Util 2022;61:102046.
- [81] Joo S, Lim C, Kwon O, Zhang L, Zhou J, Wang J-Q, Jeong HY, Sin Y, Choi S, Kim G. The first observation of Ni nanoparticle exsolution from YSZ and its application for dry reforming of methane. Mater. Reports Energ. 2021;1:100021.
- [82] Papargyriou D, Miller DN, Irvine JTS. Exsolution of Fe-Ni alloy nanoparticles from (La,Sr)(Cr,Fe,Ni)O<sub>3</sub> perovskites as potential oxygen transport membrane catalysts for methane reforming. J Mater Chem A 2019;7:15812–22.
- [83] Tang H, Dong F, Chen S, Huang J, Hong F, Su Y, bai G, Qiao B. Simultaneously boosting catalyst activity and stability by construction of low-temperature strong Metal—Support interaction. ACS Catal 2024;14:12602–9.
- [84] Xie Y, Wen J, Li Z, Chen J, Zhang Q, Ning P, Hao J. Double-edged sword effect of classical strong metal-support interaction in catalysts for CO<sub>2</sub> hydrogenation to CO, methane, and methanol. ACS Mater Lett 2023;5:2629–47.
- [85] Qiu W, Li Q, Lei Z-K, Qin Q-H, Deng W-L, Kang Y-L. The use of a carbon nanotube sensor for measuring strain by micro-Raman spectroscopy. Carbon 2013;53:161–8.